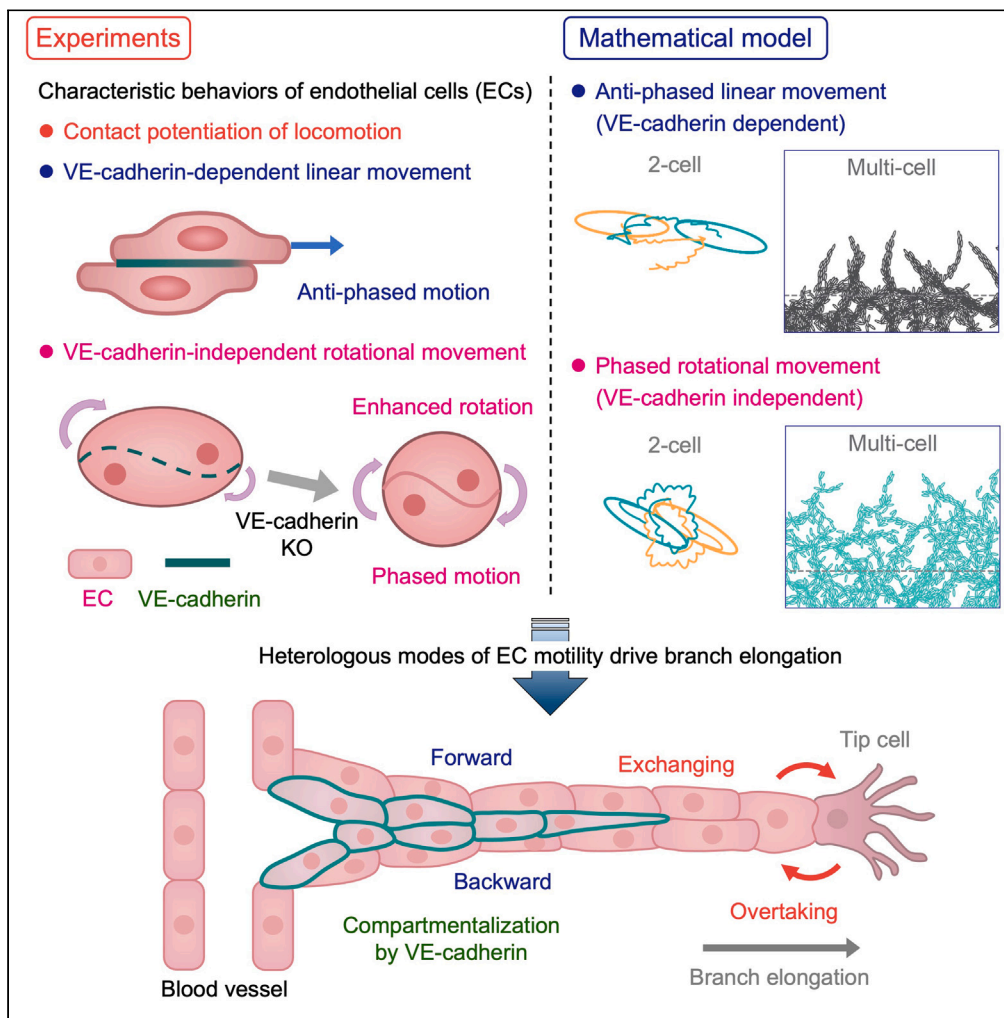## Article

Coordinated linear and rotational movements of endothelial cells compartmentalized by VE-cadherin drive angiogenic sprouting

Kazuo Tonami,
Tatsuya Hayashi,
Yasunobu
Uchijima, ...,
Yoshimitsu Kanai,
Tetsuji Tokihiro,
Hiroki Kurihara

kazutonami@gmail.com (K.T.)
kuri-tky@umin.net (H.K.)

Highlights

Contact-dependent linear and rotational movements coordinate to drive angiogenesis

VE-cadherin is required for linear motility but dispensable for rotational movement

Mathematical model based on the EC motility recapitulates angiogenic morphogenesis

VE-cadherin-dependent regional compartmentalization facilitates branch elongation

Article

Coordinated linear and rotational movements of endothelial cells compartmentalized by VE-cadherin drive angiogenic sprouting

Kazuo Tonami,[1,2,*] Tatsuya Hayashi,[2,3,4] Yasunobu Uchijima,[1] Masahiro Kanai,[5] Fumitaka Yura,[6] Jun Mada,[7] Kei Sugahara,[1] Yukiko Kurihara,[1] Yuri Kominami,[8] Toshiyuki Ushijima,[1] Naoko Takubo,[1,2,9] Xiaoxiao Liu,[1] Hideto Tozawa,[10] Yoshimitsu Kanai,[11] Tetsuji Tokihiro,[2,3,12] and Hiroki Kurihara[1,2,13,*]

SUMMARY

Angiogenesis is a sequential process to extend new blood vessels from preexisting ones by sprouting and branching. During angiogenesis, endothelial cells (ECs) exhibit inhomogeneous multicellular behaviors referred to as "cell mixing," in which ECs repetitively exchange their relative positions, but the underlying mechanism remains elusive. Here we identified the coordinated linear and rotational movements potentiated by cell-cell contact as drivers of sprouting angiogenesis using _in vitro_ and _in silico_ approaches. VE-cadherin confers the coordinated linear motility that facilitated forward sprout elongation, although it is dispensable for rotational movement, which was synchronous without VE-cadherin. Mathematical modeling recapitulated the EC motility in the two-cell state and angiogenic morphogenesis with the effects of VE-cadherin-knockout. Finally, we found that VE-cadherin-dependent EC compartmentalization potentiated branch elongations, and confirmed this by mathematical simulation. Collectively, we propose a way to understand angiogenesis, based on unique EC behavioral properties that are partially dependent on VE-cadherin function.

INTRODUCTION

In an organism, different morphological patterns are generated through sequences of cell alignment and realignment, which are often driven by collective cell migration.[1–3] Among them, the branching patterns represented by blood vessel networks are characteristic and often observed in different living systems. In the case of blood vessel morphogenesis in vertebrates, mesoderm-derived angioblasts first differentiate into vascular endothelial cells (ECs) to form the primitive vascular plexus. Then, the new blood vessels extend into surrounding avascular areas via sprouting, elongation, and branching. These two sequential processes of blood vessel formation are termed vasculogenesis and angiogenesis, respectively.[4–6]

In addition to embryonic development, angiogenesis occurs in various physiological and pathological situations such as tissue ischemia, wound healing, and tumor growth in response to tissue hypoxia and oxygen demand.[4–6] When the oxygen supply is decreased or the oxygen demand is increased, the intracellular hypoxia-sensing mechanism is activated; consequently, vascular endothelial growth factor (VEGF), the most important angiogenic factor, is produced to promote angiogenesis.[7] In this process, a population of ECs is activated by VEGF and lead the angiogenic sprouting as tip cells, followed by stalk cells, which support branch elongation through Dll4/Notch signaling.[8] Although tip and stalk cells were formerly assumed to be distinct populations, the body of research now indicates that these cells are interchangeable with complex collective cell migration referred to as "cell mixing," in which cells migrate forward and backward, passing each other even at the tip position.[9,10] This cell mixing phenomenon has been verified in _in vivo_ angiogenesis such as in mouse retinal angiogenesis.[9]

To explore the elaborate mechanism of how such inhomogeneous cell behaviors give rise to branching structures, stochastic and deterministic mathematical models have been proposed. The cell mixing phenomenon was partially recapitulated by stochastic models,[11,12] although deterministic Newtonian models with the assumption of distance-dependent attractive and repulsive two-body interactions also fit some

[1]Department of Physiological Chemistry and Metabolism, Graduate School of Medicine, The University of Tokyo, 7-3-1 Hongo, Bunkyo-ku, Tokyo 113-0033, Japan

[2]Core Research for Evolutional Science and Technology (CREST), Japan Science and Technology Agency (JST), Chiyoda-ku, Tokyo 102-0076, Japan

[3]Graduate School of Mathematical Science, The University of Tokyo, 3-8-1, Komaba, Meguro-ku, Tokyo 153-8914, Japan

[4]Faculty of Science and Engineering, Chuo University, 1-13-27 Kasuga, Bunkyo-ku, Tokyo 112-8551, Japan

[5]Department of Education and Creation Engineering, Kurume Institute of Technology, 2228-66 Kamitsu-machi, Kurume, Fukuoka 830-0052, Japan

[6]Department of Complex and Intelligent Systems, School of Systems Information Science, Future University Hakodate, 116-2 Kamedanakano-cho, Hakodate, Hokkaido 041-8655, Japan

[7]College of Industrial Technology, Nihon University, 2-11-1 Shin-ei, Narashino, Chiba 275-8576, Japan

[8]Department of Aquatic Bioscience, Graduate School of Agricultural and Life Sciences, The University of Tokyo, 1-1-1, Yayoi, Bunkyo-ku, Tokyo 113-865, Japan

[9]Isotope Science Center, The University of Tokyo, 2-11-16, Yayoi, Bunkyo-ku, Tokyo 113-0032, Japan

[10]Department of Chemistry, Graduate School of Science, the University of Tokyo, 7-3-1

Continued

aspects of collective cell migration during angiogenesis,[13,14] indicating the existence of critical cell-cell interactions driving angiogenic morphogenesis. The assumption of two-body interactions was validated by experimental data with an indication of the anisotropic nature of cell-cell interactions, which better explained EC movement during branch elongation.[15] Nevertheless, the intrinsic properties of individual cell movements that drive angiogenic morphogenesis are not fully understood.

In this study, we aimed to clarify the characteristic elements of EC motility as fundamental modules to drive angiogenesis. Through experiments on cultured ECs and mathematical modeling, we identified the enhancement of cell motility by cell-cell contact with coordinated linear and rotational movements as potential driving forces for angiogenesis. Further, we found that vascular endothelial-cadherin (VE-cadherin)[16–21] was required for the coordinated linear movement, although the rotational movement was independent of VE-cadherin. The mixture of VE-cadherin-positive and -negative ECs facilitated branch elongation with regional compartmentalization. These findings provide a mechanistic insight into angiogenic morphogenesis and the role of cadherin molecules.[22,23]

RESULTS

MS-1 murine microvascular ECs display cell mixing behaviors that drive angiogenic morphogenesis

To characterize the motility of ECs underlying angiogenic morphogenesis, we searched for appropriate cell lines that showed branch elongation with cell mixing behaviors as observed in aortic explant culture experiments.[9,15] In the Matrigel assay (see Figure S1A and STAR Methods), epithelial cells displayed sheet-forming extension retaining cell-cell contact (MDCK and COS-7 cells; Figures 1A, and S1B; Video S1), whereas mesenchymal cells tended to migrate away from each other (NIH3T3 and 10T1/2 cells; Figures 1B and S1C; Video S1), as is generally known.[24] In contrast, ECs behaved differently under the same culture conditions. In particular, MS-1 cells, an immortalized EC line derived from murine pancreatic islet microvessels,[25] exhibited typical sprouting and branch elongation without any mechanical cues such as shear stress and hydrostatic pressure (Figure 1C; Video S1). Indeed, the angiogenic potential of MS-1 cells was previously reported when co-inoculated with tumor cells into nude mice.[26] Bovine aortic ECs displayed sheet formation with fine protrusions at the front (Figure S1D). Human umbilical vein ECs (HUVECs) formed characteristic tube-like network structures instead of branching (Figures S1E and S1F). Notably, Vero cells, although not ECs, also showed fine branch formation, suggesting that these cells may also possess some behavioral properties common to ECs (Figure S1G). These observations led us to focus on the motility of MS-1 cells in comparison to other ECs and non-endothelial cells.

Time-lapse imaging demonstrated that MS-1 cells moved forward and backward with repetitive cellular overtaking and frequent replacement of tip cells during branch elongation (Figures 1D–1F; Video S2), similar to cell mixing behaviors in the mouse aortic explant assay.[9,15] In our previous study, we found anisotropic interaction between forward- and backward-moving cells, which resulted in accelerated cell movement when the cells passed each other.[15] Consistently, cell speed was increased when cells were passing in the branch elongation of MS-1 cells (Figures 1G and 1H) as well as in the aortic explant assay (Figures S1H and S1I) at both the stalk and tip positions. These results provide validation that the cell motility analysis of MS-1 cells is appropriate for the present purpose.

MS-1 cells display contact-dependent enhancement of motility in a two-cell state

To investigate the fundamental processes underlying angiogenesis, we analyzed the interactive behaviors of ECs and non-ECs in a two-cell state after cell division. In general, cells tend to cease motility or move away from each other upon collision, a process that is known as contact inhibition of locomotion (CIL).[24,27] As expected, mesenchymal cells such as NIH3T3cells and 10T1/2 cells moved apart from each other and migrated randomly with increased migration speed after cell division (Figures 2A and S2A; Video S3), whereas epithelial cells, such as Madin-Darby canine kidney (MDCK) cells and Vero cells attenuated their movement maintaining contact with each other (Figure 2B and S2B; Video S3). In contrast, MS-1 cells displayed enhanced motility with rotational movement and directional motion maintaining contact after cell division (Figure 2C; Video S4). Such enhancement of cell motility in paired daughter cells after division was also observed in HUVECs, although they tended to detach from each other more frequently than MS-1 cells (Figures S2D and S2E; Video S5). COS7 cells, non-endothelial cells that form sheets in Matrigel, also upregulate cell motility upon cell-cell contact (Figures S2C; Video S6), although they did not display a

Hongo, Bunkyo-ku, Tokyo 113-0033, Japan

[11]Cell Biology and Anatomy, Graduate School of Medicine, Wakayama Medical University, 811-1 Kimiidera, Wakayama 641-8509, Japan

[12]Department of Mathematical Engineering, Faculty of Engineering, Musashino University, 3-3-3 Ariake, Koto-ku, Tokyo 135-8181, Japan

[13]Lead contact

*Correspondence: kazutonami@gmail.com (K.T.), kuri-tky@umin.net (H.K.)

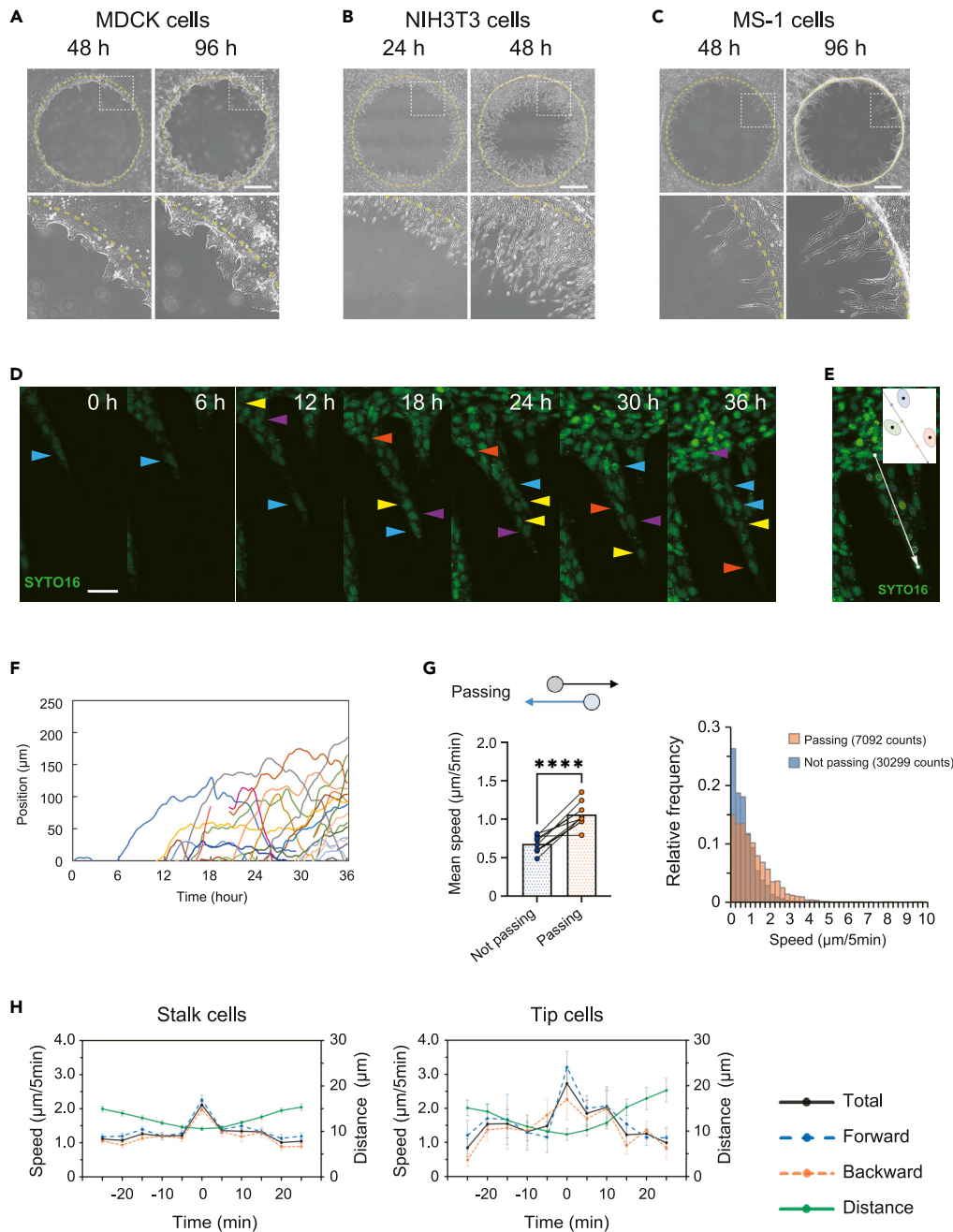https://doi.org/10.1016/j.isci.2023.107051

Figure 1. MS-1 cells exhibit angiogenic sprouting with cell mixing

(A–C) Phase-contrast images of MDCK (A), NIH3T3 (B), and MS-1 (C) cells migrating into Matrigel at the indicated times after seeding. Scale bars represent 1000 μm. See also Video S1.

(D) Time-lapse sequences of migrating MS-1 cells in Matrigel. Cell nuclei were visualized by SYTO16 staining. Each colored arrowhead tracks the movement of an individual cell located at the tip position. Scale bar represents 50 μm. See also Video S2.

(E and F) Time evolution of individual cell positions in (D). Each line with different color (F) represents the trajectory of an individual EC along the axis of elongation (white arrow in E).

(G) Comparison of the mean (left) and distribution (right) of migration speed between cells at the state of "Passing" or "Not passing", as defined in STAR Methods. Data were extracted from 36-h trajectories of all analyzed cells in 10 elongating branches (also in H). Data are represented as scatterplots with bars indicating means. ****p < 0.0001, paired t test.

(H) Changes in the mean instantaneous speed of stalk and tip cells around the time of "Passing". Data are represented as mean ± SEM for each time point.
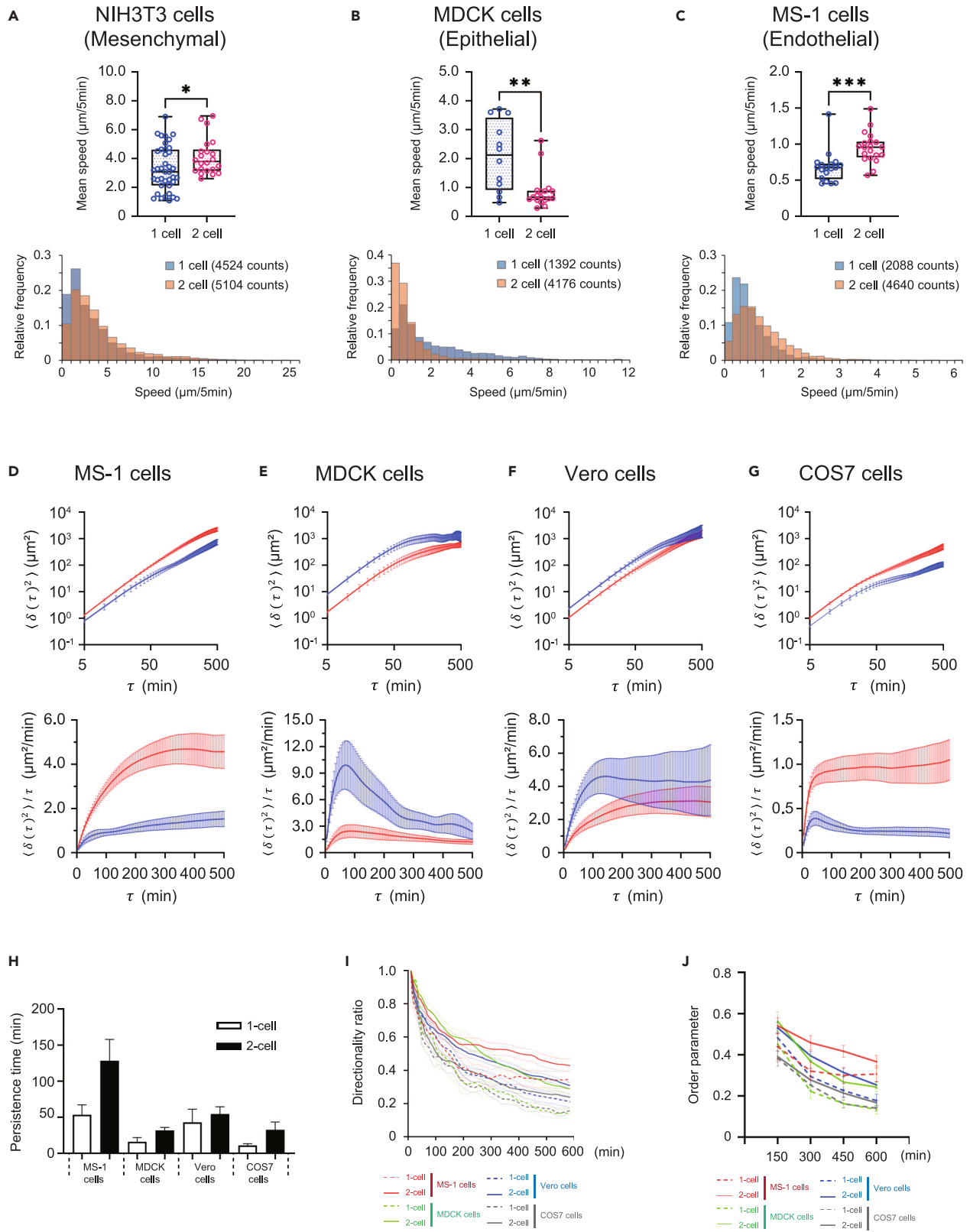
Figure 2. Analysis of the directional motility of ECs and non-ECs at a two-cell state

(A–C) Boxplots of mean speeds (upper) and histograms of their distribution (lower) in NIH3T3 (1-cell, n = 39; 2-cell, n = 22) (A), MDCK (1-cell, n = 12; 2-cell, n = 18) (B), and MS-1 (1-cell, n = 18; 2-cell, n = 20) (C) cells in one- and two-cell states. Mean speed at a two-cell state was calculated as an average speed of each cell pair. Data are represented as box-whisker plots. *p < 0.05, **p < 0.01, ***p < 0.001, Welch's t-test.

(D–G) Averaged MSD ($\langle\delta(\tau)^2\rangle$) (upper) and MSD divided by time interval τ (lower) plotted on log-log and linear scales, respectively, in MS-1 (1-cell, n = 18; 2-cell, n = 40) (D), MDCK (1-cell, n = 12; 2-cell, n = 36) (E), Vero (1-cell, n = 32; 2-cell, n = 82) (F), and COS7 (1-cell, n = 24; 2-cell, n = 60) (G) cells. Blue and red lines represent 1-cell and 2-cell states, respectively.

(H) Persistence time estimated from the averaged MSD data.

(I) Directionality ratio over elapsed time t (min).

(J) Order parameter measured in the indicated time interval. Trajectories obtained from time-lapse images for 10 h from 2 h after the onset of anaphase were analyzed here. Data in (D–J) are represented as mean ± SEM.

branching pattern (Figure S1B), leading us to speculate that there are further distinctive features necessary for branching morphology.

Coordinated linear and rotational movements characterize EC behaviors

As MS-1 cells appear to migrate more directionally in a two-cell state after cell division (Video S4), we investigated the directional persistence and the straightness of cell movement to characterize EC behaviors. To assess the impact of cell-cell contact, we compared MS-1 cells with non-EC cells, which keep their contacts in a two-cell state after cell division. We used three measures derived from cell trajectories to evaluate directional motility: mean square displacement (MSD), directionality ratio (DR), and order parameter (OP)[28–30] (see STAR Methods). For each cell type, MSDs were averaged to obtain an ensemble-averaged MSD ($\langle\delta(\tau)^2\rangle$), which is shown as plots of $\langle\delta(\tau)^2\rangle$ and $\langle\delta(\tau)^2\rangle/\tau$ versus time (τ) in Figures 2D–2G. The term $\langle\delta(\tau)^2\rangle/\tau$ is constant for a random walk behavior, whereas the slope of $\langle\delta(\tau)^2\rangle/\tau$ vs. τ is 1 for cells in ballistic movement.[31–33] The directional persistence time, calculated from the data as the crossover time from ballistic to a random-walk behavior, was higher in MS-1 cells than in other cell types, and was much increased in a two-cell state, suggesting that MS-1 cells tend to move with a higher persistence through cell-cell contact (Figure 2H). The enhanced directional persistence of MS-1 cells in a two-cell state was also supported by a higher DR (Figure 2I) and OP (Figure 2J). Collectively, MS-1 cells characteristically display coordinated linear movement upon cell-cell contact, which may drive directional branch elongation.

In addition to the coordinated linear movement, we identified unique rotational movement around the cell-cell interface in paired MS-1 cells after cell division (Figures 3A and 3B; see also Video S4). This pattern of movement may correspond to passing and exchanging cell behaviors at the tip and stalk positions in angiogenesis. Such rotational movement was also observed in other ECs such as primary cultured mouse brain microvascular ECs (Video S7). Vero cells, which are not ECs but form fine branches (Figure S1G), also exhibited rotational movement in a two-cell state (Video S7), suggesting a relationship between rotational movement and branch formation. During the rotational movement, MS-1 cells tended to move faster as they became closer to each other (Figure 3C), forming a relative velocity angle mostly within 120°–180° (Figure 3C). When the rotational movement was defined as the movement keeping the relative velocity angle within 120°–180° for more than an hour, the ratio of rotational time to total time was exceptionally high in MS-1 cells compared with other cells examined (Figure 3D). The higher cell speed during the rotational movement of MS-1 cells was statistically verified under this definition (Figures 3E and 3F). Because rotating cells move antiparallel to each other in direction, this phenomenon likely corresponds to the accelerated cell movement that occurs when passing each other during angiogenic sprouting.[15] Indeed, similar acceleration in passing cells was also observed in MS-1 cells at both the tip and stalk positions during branch elongation in Matrigel (Figures 1G and 1H, S1H and S1I).

Collectively, coordinated linear and rotational movements, dependent on cell-cell contact, can characterize EC movements. Coordinated linear movement may contribute to the alignment of movement, whereas the accelerated antiparallel movement represented by paired cell rotation may provide a driving force for branch elongation, as evidenced by previous mathematical simulations.[15]

VE-cadherin is required for coordinated linear movement and branching morphogenesis

Directional linear movement and fast rotational movement upon cell-cell contact are likely mediated by cell adhesion molecules. Because molecules of the cadherin family regulate coordinated cell migration including CIL and the epithelial-mesenchymal transition (EMT) emerging through cell-cell
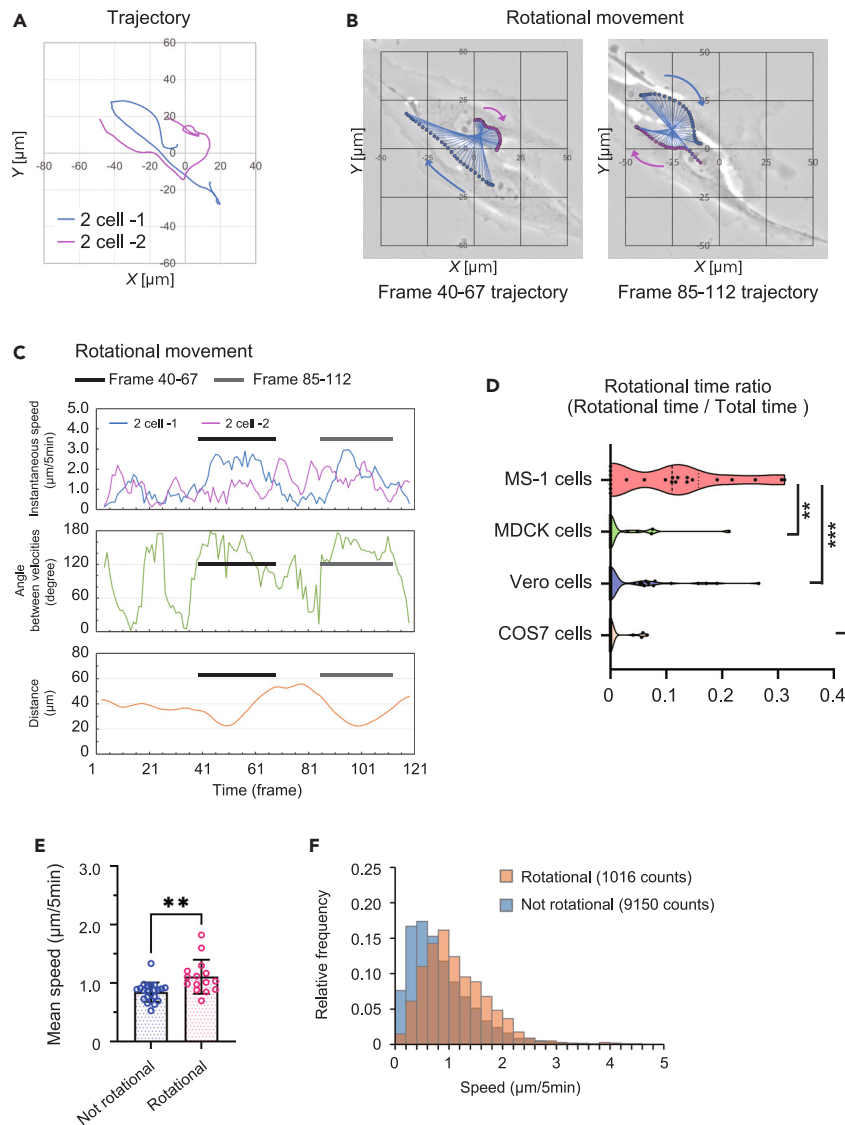
Figure 3. ECs exhibit fast rotational movement in a two-cell state

(A) A representative trajectory of paired ECs showing rotational movement.

(B) Tracking of rotational movements of ECs. Arrows indicate the direction of cellular rotation with blue lines connecting cell pairs at the same time.

(C) Time evolution of instantaneous speed (top), angle between the velocities (middle), and internuclear distance (bottom) of the representative rotating cell pair (the same as in A and B) for 10 h.

(D) Comparison of rotational time ratio between MS-1 ECs (n = 22) and other adherent cells (MDCK, n = 19; Vero, n = 46; COS7, n = 30). Total trajectories obtained from time-lapse images within 48 h were analyzed. Data are represented as violin plots. **p < 0.01, ***p < 0.001, ****p < 0.0001, Kruskal-Wallis test and Dunn's test.

(E and F) Comparison of mean speeds (E) and their distribution (F) between cells in the "Rotational" or "Not rotational" state. Data are represented as scatterplots with bars indicating means ± SEM. **p < 0.01, Welch's t-test.

interaction,[24,34–36] we focused on VE-cadherin to elucidate the molecular mechanism underlying the behavioral properties unique to ECs. VE-cadherin distribute with comb-shaped and dot-like patterns at the interface between MS-1 cells (Figure 4A and S3A) as seen in primary ECs and HUVECs.[37,38] We generated VE-cadherin-knockout (KO) MS-1 cells using CRISPR-Cas9 technology. The successful deletion of the VE-cadherin protein was confirmed by immunocytochemistry and Western blotting analysis with anti-VE-cadherin antibody (Figures 4A, and S3B). VE-cadherin-KO MS-1 cells appear to lose cell polarity and become round in shape, whereas wild-type MS-1 cells were coordinately aligned (Figure S3C). Within
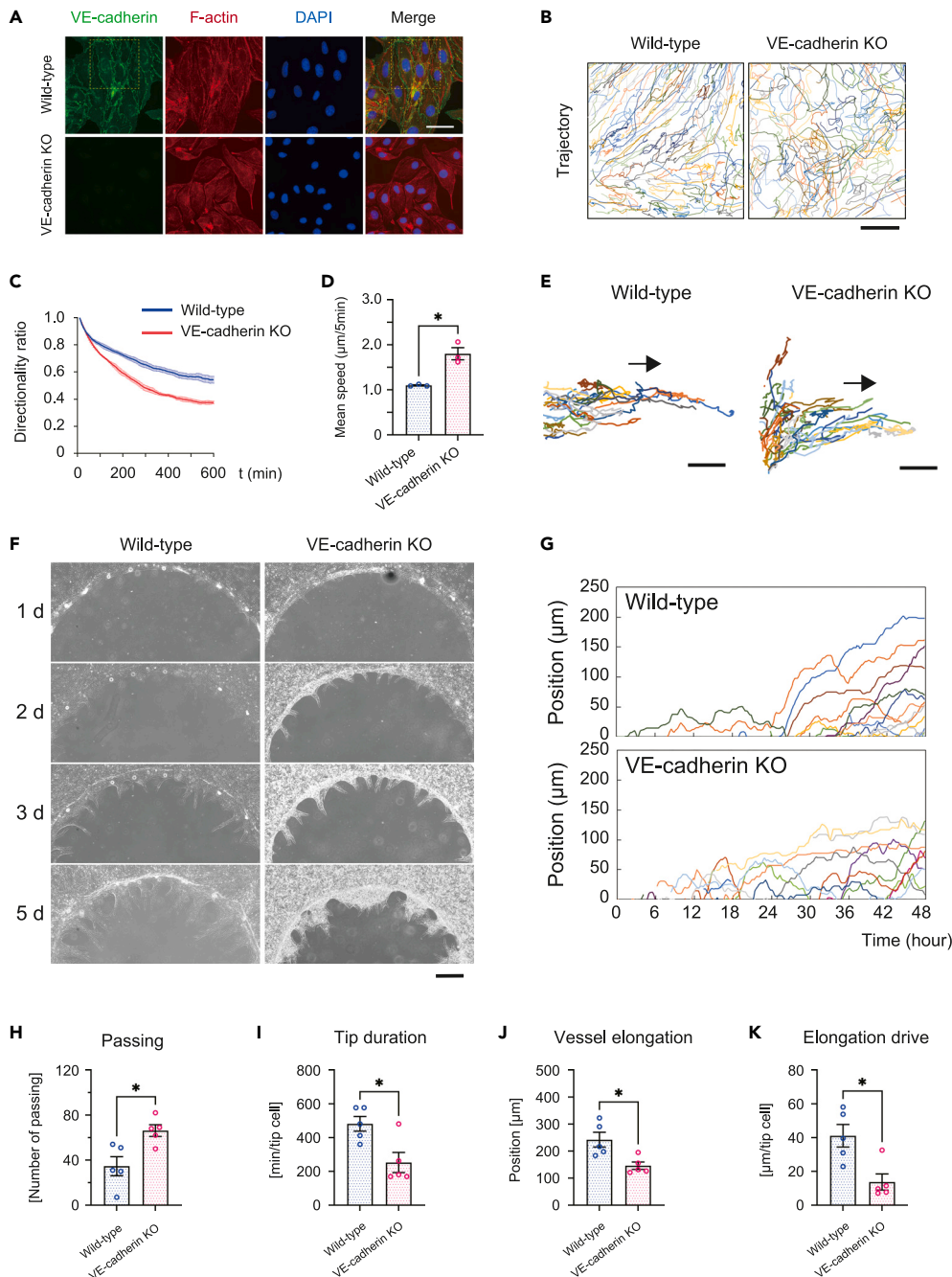
Figure 4. VE-cadherin is required for the coordinated linear movement that facilitates forward sprout elongation

(A) Triple staining of wild-type and VE-cadherin-KO MS-1 cells with anti-VE-cadherin antibody (green), F-actin-binding fluorescent phalloidin (red), and DAPI (blue). Scale bar represents 50 μm.

(B) Trajectories of wild-type and VE-cadherin-KO MS-1 cells within high-density monolayers (ECM-free region) from 48 to 60 h after seeding. Scale bar represents 50 μm.

(C and D) Directionality ratio (C) and mean speed (D) of wild-type and VE-cadherin-KO MS-1 cells migrating within monolayers from 24 to 72 h after seeded. Mean values were obtained from three independent experiments. Data are represented as mean ± SEM for each time point (C) or scatterplots with bars indicating means ± SEM (D). *p < 0.05, Welch's t-test.

(E–K) Angiogenic sprouting of wild-type and VE-cadherin-KO MS-1 cells in the Matrigel assay. (E) Trajectories of individual ECs from 48 to 72 h after seeding. Scale bars represent 50 μm. (F) Phase-contrast images of migrating cells at the indicated days after seeding. Scale bar represents 500 μm. (G) Time evolution of individual EC positions along the axis

Figure 4. *Continued*

of elongation from 24 to 72 h after seeding. (H–K) Comparison of cell motility parameters (defined in STAR Methods). Data were obtained from five branches for each group. Data are represented as scatter plots with bars indicating means ± SEM. *p < 0.05, Welch's t-test.

high-density monolayers, wild-type MS-1 cells show streams of widely coordinated cell movement (Figure 4B), as reported previously.[38] In contrast, in VE-cadherin-KO, migration directionality decreased but cell speed was enhanced (Figures 4B–4D). In angiogenic sprouting, VE-cadherin-KO in MS-1 cells deteriorated proper branch elongation, resulting in collapsed branch structure (Figures 4E, 4F, S3D, and S3E; Video S8), although typical cell mixing phenomena including tip cell exchanging were still observed (Figure 4G) with increased frequency of cell passing (Figure 4H). When tip cell behaviors were evaluated using tip cell parameters that we previously defined,[9] "tip duration" (the time spent per tip cell) was significantly decreased in VE-cadherin-KO cells, indicating increased frequency of tip cell exchanging (Figure 4I), whereas "vessel elongation" was decreased (Figure 4J). As a consequence, "elongation drive" (displacement per tip cell) was significantly attenuated (Figure 4K).

Altogether, these findings indicate that VE-cadherin is required for coordinated linear movements that facilitate forward sprout elongation, although it may negatively regulate the passing of ECs upon cell-cell contact and the to-and-fro movement in branch elongation.

VE-cadherin-knockout enhances synchronized rotational movements

Subsequently, we aimed to determine how VE-cadherin-KO affected the behaviors of MS-1 cells in a paired cell state after cell division. The characteristic linear and rotational movement of MS-1 cells was accompanied by lamellipodial formation at the cell-cell interface as well as outward lamellipodial protrusion, as observed by actin dynamics visualized with LifeAct-RFP[39] (Figures 5A and 5A'). The rotational movement was predominant in VE-cadherin-KO MS-1 cells with enhanced lamellipodial formation involving the cell-cell interface at the expense of aligned linear movement (Figures 5B, 5B', and 5C; Video S9). During paired cell movement, cell-cell adhesion was maintained in the absence of VE-cadherin, possibly by other cell adhesion molecules such as platelet endothelial cell adhesion molecule 1 (PECAM1)[40] (Figure S4A). The enhancement of the rotational movement in a two-cell state is consistent with increased cellular passing in angiogenesis (Figures 4H and 4I), which is likely driven by adhesion molecules other than VE-cadherin.

Further, we observed that the rotational movement of paired VE-cadherin-KO MS-1 cells was characterized by phase synchronization (Figure 5D; Video S10), which was quantitatively ascertained by Pearson's correlation coefficient between the time series velocity fluctuations of paired two-cells (Figure 5E). Such synchronization was not observed in wild-type MS-1 cells, which instead showed occasional anti-phased movement, especially when either of the two cells moved fast, as indicated by arrows in Figure 5D. The property of anti-phased motion in wild-type two-cells was reflected by the asymmetric distribution of integrin-mediated focal adhesions (FAs) stained with vinculin,[41–43] which were associated with well-aligned actin fibers in the cell periphery. By contrast, FAs were localized throughout the cell body in a symmetric fashion in paired VE-cadherin-KO cells (Figures S4B–S4D).

To confirm the role of VE-cadherin in endothelial motility, we transfected VE-cadherin-KO MS-1 cells with VE-cadherin-EGFP. Decreased directionality of VE-cadherin-KO MS-1 cell movement was rescued by VE-cadherin-EGFP (Figure 5F; Video S10). Enhanced cell speed and rotational movement in VE-cadherin-KO cells were also decreased to levels comparable with wild-type cells (Figures 5G and 5H). By contrast, endocytosis-defective VE-cadherin mutant (VE-cadherin-DEEmut-EGFP)[44] did not rescue the VE-cadherin-KO phenotype (Figures 5F–5G; Video S10), consistent with previous report that VE-cadherin endocytosis is required for collective cell movement during angiogenesis.[37,38] Notably, transfection of wild-type MS-1 cells with VE-cadherin-EGFP hindered cell movement (Video S11), indicating that optimal VE-cadherin levels are essential for directional linear movement.

Collectively, these results indicate that directional linear and rotational movements are conferred by VE-cadherin-dependent and -independent mechanisms, respectively. In addition, VE-cadherin may negatively regulate rotational movement and its synchronicity.
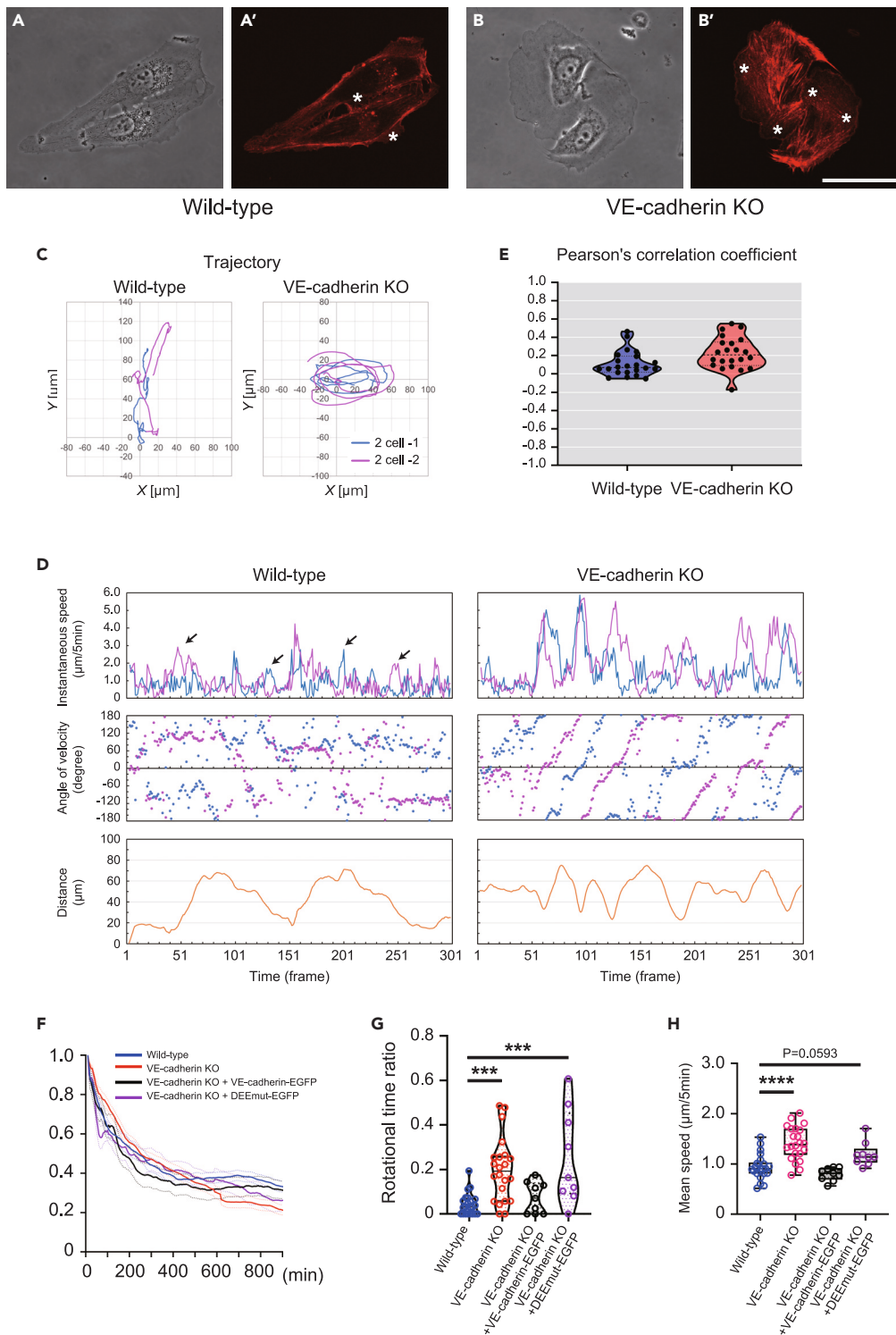
Figure 5. Synchronized rotational movement was enhanced by VE-cadherin KO

(A–B′) Phase-contrast images (A and B) and F-actin labeling by LifeAct-RFP (A′ and B′) of wild-type (A and A′) and VE-cadherin-KO MS-1 cells (B and B′). Scale bar represents 50 μm.

(C) Representative trajectories of wild-type and VE-cadherin-KO MS-1 cells on 2-cell interplay for 25 h. See also Video S10.

(D) Time evolution of instantaneous speed, angle of velocity, and spatial distance between a representative cell pair. Paired cells are represented by blue and red plots.

Figure 5. *Continued*

(E) Violin plot showing Pearson's correlation coefficient between the instantaneous speeds in wild-type (n = 22) and VE-cadherin-KO (n = 22) pairs.

(F–H) Comparison of directionality ratio over elapsed time t (min) (F), rotational time ratio (rotational time per total time) (G), and mean speeds (H) among wild-type cells (n = 22), VE-cadherin-KO cells (n = 22), and VE-cadherin-KO cells transfected with VE-cadherin-EGFP (n = 9) or VE-cadherin-DEEmut-EGFP (n = 9) in two-cell states. n indicates a number of paired cells. Mean speed at a two-cell state was calculated as an average speed of each cell pair. Data are represented as violin plots (G) or box-whisker plots (H). ***p < 0.001, ****p < 0.0001, one-way ANOVA and Dunnett's test.

Mathematical modeling based on cell behaviors recapitulates angiogenic morphogenesis and the effects of VE-cadherin-knockout

To substantiate the characteristic EC behaviors that we identified as processes fundamental to angiogenesis, we developed a mathematical model of angiogenesis incorporating the cohesive and phasic nature of rotational movement into a two-dimensional elliptic particle model based on previous models, in which distance-dependent attractive and repulsive two-body interaction reproduced sprouting and elongation with cell-mixing phenomenon.[14,45] Specifically, we introduced additional variables, such as the self-driving force D_i^t and the internal variable ϕ_i^t representing the anti-phase synchronization in paired ECs, which was assumed to be zero in single ECs and VE-cadherin-KO ECs. The present model also differed from the previous model as the rotation variable ψ_i^t was set to align the long axis to the direction of movement (Figures S5A–S5H). As a parameter to determine ψ_i^t, two magnitudes of rotational forces were employed as γ_1 = 0.02 (moderate) and 0.05 (strong) in VE-cadherin-KO cells. The movement of paired wild-type cells is constituted by the typical anti-phasic translational movement, and that of VE-cadherin-KO cells follows the rotational movement with both magnitudes of rotational forces (Figure 6A; Video S12). Our numerical simulation of two-cell behaviors shows that pairs of wild-type cells display more directional movement than those of VE-cadherin-KO cells (Figure 6B), whereas VE-cadherin-KO cells had a higher speed than that of the experiments (Figure S5I), as observed in *in vitro* experiments.

Next, we performed numerical simulations of the dynamics of sheet-forming EC layers. The time evolution under the conditions mimicking wild-type ECs revealed multiple branch formation toward a cell-free area, whereas the condition mimicking VE-cadherin-KO cells resulted in twisted and fused branches with moderate rotation although migration speed was increased (Figures 6C, and S5J; Video S13). These features of branch structures recapitulated experimental observations (Figure 4F). Under the conditions for strong rotation, branch formation was mostly abrogated (Figure 6C; Video S13). Furthermore, our simulation successfully reproduced the "cell mixing" phenomenon, with cells passing each other and overtaking at the tip and stalk positions (Figure 6D; Video S13), with the migration speed of passing cells enhanced as in experimental observations (Figures 6E and S5K). The cell mixing was also reproduced in the simulation of VE-cadherin-KO cells (Figures 6F, 6G, and S5K) with increased cell passing and decreased tip duration as in experimental results (Figures 6H and 6I).

Then, we examined how cell shape influenced the branch structure in our mathematical model, because VE-cadherin-KO cells were round in shape compared with wild-type cells, in addition to their changed motility (Figure S5L). Simultaneously, we examined the impacts of motion phase and rotational force in this test shown as the catalogs of numerically simulated branch structures (Figures S5M and S5N). In terms of the nature of cell motilities, the motion phase impacted the directionality of branch elongation; phased motion increased branch elongations, but twisted them (Figure S5N), whereas more linear branches were formed with anti-phased motion (Figure S5M). Rotational force affected branch structures; as the rotational force γ_1 increased over 0.02, the branch structures broke down in both anti-phased and phased motion (Figures S5M and S5N). With regard to cell shape, decreases in oblateness (χ) dampened forward collective migration with sprouting and branching (Figures S5M and S5N) in both wild-type and VE-cadherin-KO ECs. Although the elliptic particle in the present model does not simply reflect cell morphology, this result suggests that cell shape, including a kind of force field, may be a determinant of the branching patterns generated by collective cell migration involving "cell mixing."

Thus, our mathematical model incorporating the properties of the rotational movement and motion phase successfully reproduced angiogenic sprouting through the directional migration and dynamic cell mixing phenomenon, indicating that the characteristic behaviors identified in the paired cell experiments are fundamental modules of angiogenesis.
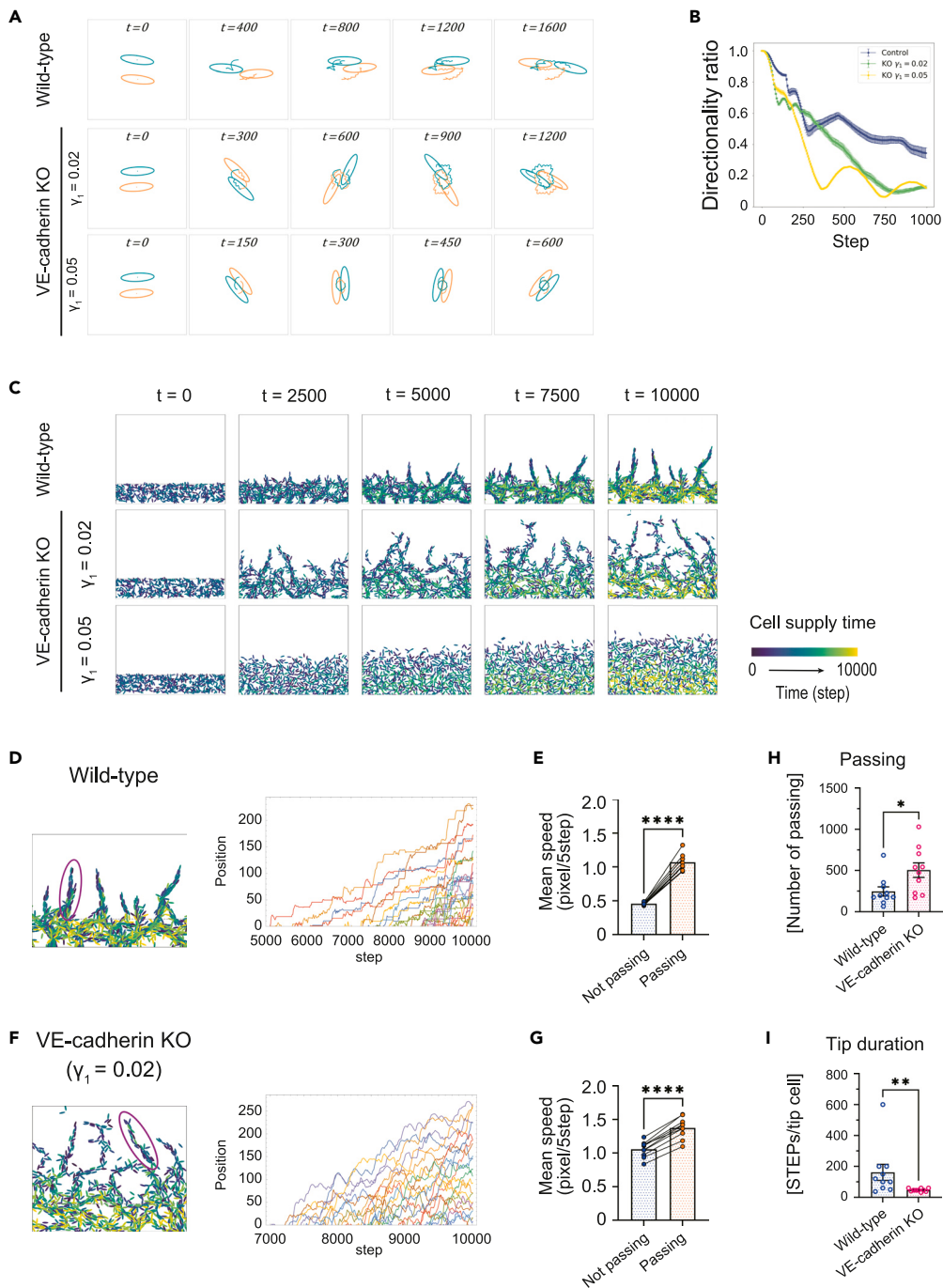
Figure 6. Mathematical model and numerical simulation

(A) Representative numerical simulation of the dynamics of wild-type and VE-cadherin- KO (γ_1 = 0.02 and 0.05) cell pairs. Wild-type cells alternately move and stop, while VE-cadherin-KO cells rotate synchronously. See also Video S12.

(B) Directionality ratio of wild-type and VE-cadherin-KO cell pairs.

(C) Representative snapshots of collective cell migration in the numerical simulation with the parameters used in (A). Cells were supplied from the bottom area at different time steps indicated by color. See also Video S13.

(D–G) Trajectory analysis of simulation results in (C). Individual cell positions in circled branches were projected onto the elongation axis (D and F) and the mean speeds were compared between cells at the state of "Passing" or "Not passing" (E and G) in wild-type (D and E) and VE-cadherin-KO (F and G) cells.

Figure 6. Continued

(H and I) Comparison of the number of passing (H) and tip duration (I). STEPs in (I) is 5 steps. The plots in (E–I) are averaged over 10 simulations. Details of the mathematical modeling are described in STAR Methods. Data are represented as scatterplots with bars indicating means (E and G) or means ± SEM (H, I). ****p < 0.0001, paired t-test (E and G), *p < 0.05, **p < 0.01, Mann-Whitney U test (H and I).

VE-cadherin-dependent compartmentalization of angiogenic ECs

The expression and distribution of VE-cadherin are heterogeneous among ECs and change dynamically during sprouting angiogenesis,[46] which may be related to different behavioral modules. Indeed, MS-1 ECs forming angiogenic branches in Matrigel had heterogeneous VE-cadherin expression, whereby ECs with high VE-cadherin expression were located in the center of branches (Figures 7A and S6A). To test how the heterogeneity of VE-cadherin expression affected angiogenic sprouting and branching, we admixed wild-type and VE-cadherin-KO ECs at different ratios and evaluated the time evolution of sprouting and branching. Consequently, sprouting and branch elongation were promoted by admixing wild-type and VE-cadherin-KO ECs in a 4:1 ratio (Figures 7B–7E, and S6B), whereas the number of sprouts was ultimately not affected (Figure 7F). The mixture of wild-type and VE-cadherin-KO ECs in a 1:1 ratio also increased the area of sprouts, but the increase in the length of sprouts was not significant (Figures 7B–7E and S6B). Immunostaining for VE-cadherin revealed that wild-type (VE-cadherin-positive) cells were compartmentalized at inner regions, whereas VE-cadherin-KO (VE-cadherin-negative) cells were located at the outer and tip regions in the branches composed of 4:1 and 1:1 cell mixtures, consistent with the VE-cadherin expression pattern in wild-type ECs (Figures 7A and S6A). These results suggest that the heterogeneity of VE-cadherin expression in ECs promotes branch elongation with compartmentalization in angiogenesis.

To determine whether the effect of the heterogeneity of VE-cadherin expression on branch formation could be explained by the different parameters of the mathematical model, we performed numerical simulations for the dynamics of sheet-forming cell layers composed of a mixture of wild-type and VE-cadherin KO ECs. This admixing of wild-type and VE-cadherin-KO cells reproductively facilitated branch elongation (Figures 7G–7I; Video S14) while decreasing the linearity of branches (Figure 7J). The number of sprouts was not affected by cellular heterogeneity (Figure 7K). Interestingly, wild-type and VE-cadherin-KO cells were also compartmentalized in the mathematical model when homophilic binding affinity was not included. In this numerical simulation, wild-type cells segregated at the inner region of branches and VE-cadherin-KO cells tended to occupy tip cells (Figure 7G; Video S14) similar to experimental results. Similar results were obtained using round-shaped cells (χ = 0.6) mimicking VE-cadherin-KO ECs (Figures S6C–S6G).

Collectively, the heterogeneity of ECs with different behavioral properties can prompt branch elongation with compartmentalization, which is not necessarily dependent on the differences in homophilic binding mediated by cadherin molecules.

DISCUSSION

In this study, we identified the coordinated linear and rotational movements potentiated upon cell-cell contact as fundamental behavioral modules of angiogenesis. Further, we found that VE-cadherin was required for the coordinated linear motility but dispensable for the characteristic rotational movement of ECs. VE-cadherin-KO rather enhanced the rotational movement, in which ECs exhibited synchronized motion, indicating that VE-cadherin may regulate rotatory and synchronous motility to rectify linear branch elongation, as suggested by mathematical simulations. Finally, a mixture of VE-cadherin-positive and -negative ECs was found to facilitate branch elongation with regional compartmentalization.

Contact-dependent enhancement of motility in ECs

In contrast to CIL, contact-dependent enhancement of motility has been reported as a unique mode of cell movement in various cell types, such as human astrocytoma cells[47] and spreading colonies of *Dictyostelium discoideum* cells.[48] Astrocytoma cells, upon OL-protocadherin overexpression or N-cadherin knockdown, accelerate their movement when they contact with neighbor cells, separating from one another soon thereafter.[47] *D. discoideum* cells enhance ameboid motility without cell adhesion.[48] In contrast, ECs showed a different mode of motility enhancement, in which ECs maintain cell-cell contact as if crawling along one another. ECs form lamellipodial protrusions at the cell-cell interface, as well as outwards in a two-cell state,
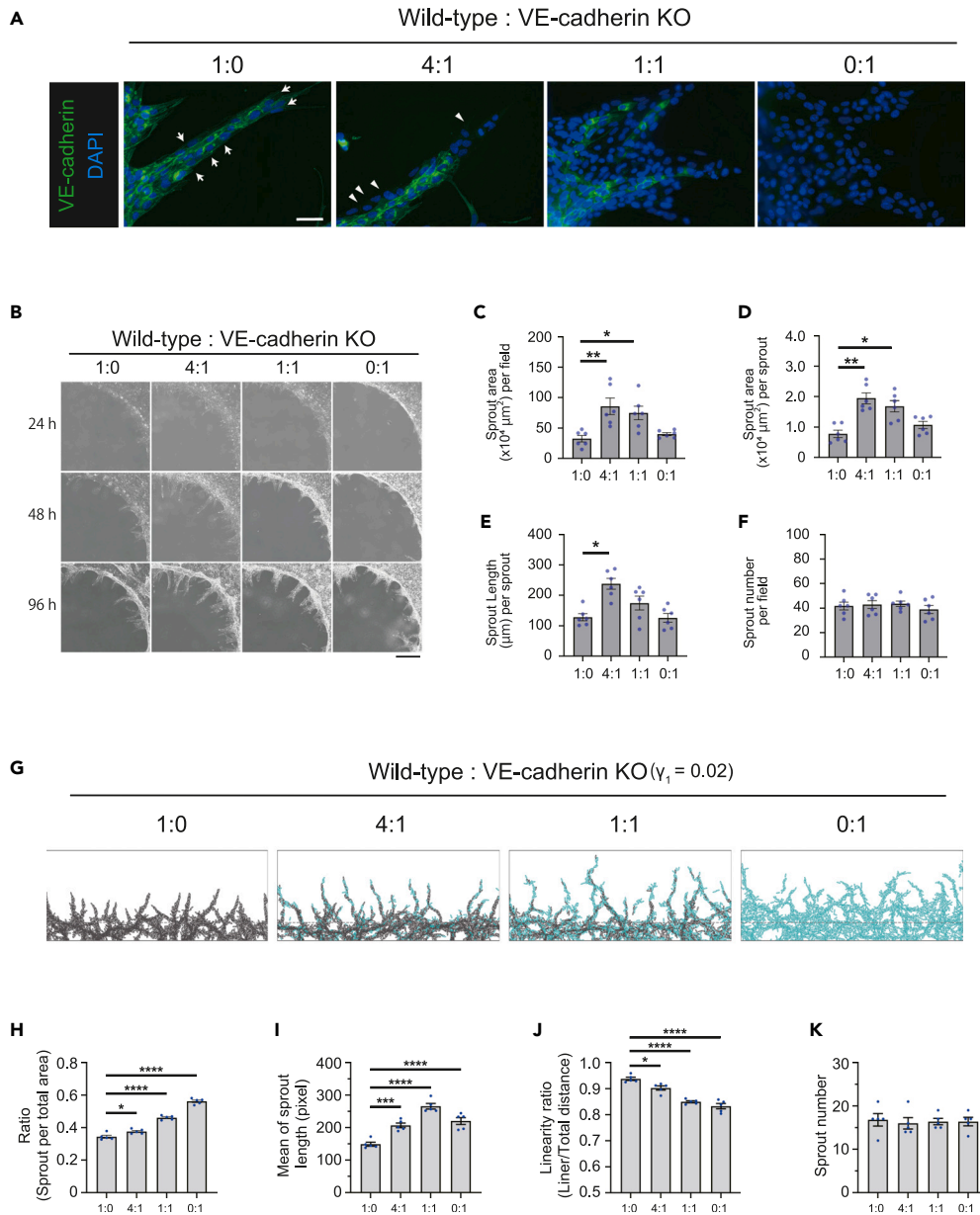
Figure 7. VE-cadherin-dependent compartmentalization of angiogenic ECs

(A) Staining with anti-VE-cadherin antibody (green) and DAPI (blue) for angiogenic branches containing wild-type and VE-cadherin-KO MS-1 cells at indicated ratios. Samples were fixed 96 h after assays were started. Arrowheads indicate VE-cadherin- KO cells. Scale bar represents 50 μm.

(B) Phase-contrast images of angiogenic sprouting of MS-1 cells in Matrigel at the indicated times after seeding. Wild-type and VE-cadherin-KO MS-1 cells were mixed at indicated ratios. Scale bar represents 500 μm.

(C–F) Quantification of angiogenic parameters in sprouts 48 h after seeding (n = 6 for each group). Data are represented as scatterplots with bars indicating means ± SEM. *p < 0.05, **p < 0.01, Kruskal-Wallis test and Dunn's test.

(G) Simulation of branching morphogenesis with the mathematical model, in which wild-type (black) and VE-cadherin-KO (turquoise) cells were mixed at indicated ratios.

(H–K) Quantification of angiogenic parameters in simulated angiogenic sprouts (n = 5 for each group). Data are represented as scatterplots with bars indicating means ± SEM. *p < 0.05, ***p < 0.001, ****p < 0.0001, one-way ANOVA and Dunnett's test.

whereas cells undergoing CIL and astrocytoma cells form lamellipodial protrusions in directions opposite to the contact site. Considering that the inactivation of Rac1 abrogates lamellipodial formation at the contact site in the process of CIL,[49,50] the present results indicate that Rac1 may be activated at the contact site in ECs, which could antagonize the CIL machinery, if present.

Coordinated linear and rotational movement of ECs

We also identified VE-cadherin-dependent coordinated linear and VE-cadherin-independent rotational movements as characteristic elements of EC motility. The rotational movement in VE-cadherin-KO MS-1 cells was accompanied by enhanced lamellipodial formation including at the contact site, indicating that lamellipodial formation along each other drives rotational movement and VE-cadherin may suppress it to enhance linear movement in the parallel direction to each other. In addition, the rotational movement of VE-cadherin-KO MS-1 cells was different from that of wild-type cells in terms of the synchronicity. VE-cadherin likely confers paired cells with asymmetric distribution of FAs, in which one cell may act as a scaffold for the other. Numerical simulation in the present mathematical model supported the idea that these behavioral characteristics constitute angiogenic modules in which VE-cadherin facilitates efficient forward elongation by ensuring linearity and asynchrony.

VE-cadherin has been proven essential for vascular development and morphogenesis,[51–53] whereas a moderate decrease in VE-cadherin expression induces hypersprouting due to failure to suppress VEGFR2/Rac1-dependent sprout formation.[54,55] Conversely, excessive VE-cadherin expression suppresses cell movement as shown in this study. These findings suggest that the modulation of VE-cadherin expression on the cell surface is critical for appropriate angiogenesis. Furthermore, we also found that heterogeneity in VE-cadherin function may optimize angiogenic branch elongation by using an admixing culture of wild-type and VE-cadherin-KO cells and numerical simulation. Thus, VE-cadherin may regulate the interactive cell migration of ECs between linear and rotational movements with different synchronicity, leading to fine-tuned branch elongation.

VE-cadherin undergoes clathrin-dependent endocytosis, which controls the directional migration of ECs essential for angiogenesis, as well as vascular integrity.[37,56] Engulfed cadherin fingers and VE-cadherin plaques are reported to drive coordinated directional migration of ECs via actin polymerization.[38,57] In addition, the clathrin-independent transcellular endocytosis of VE-cadherin has been found as a form of cell-cell communication.[58] The present result that VE-cadherin endocytosis is required for linear directional movement is consistent with these previous findings. Further investigation of how these VE-cadherin dynamics link to the modulation of angiogenic processes through the different modes of EC motility is required.

VE-cadherin-dependent compartmentalization of ECs in angiogenesis

We found that ECs were compartmentalized according to different expressions of VE-cadherin. Interestingly, our mathematical model incorporating the properties of cell movements, but not homophilic binding affinity recapitulated this compartmentalization, suggesting that differential properties of motility can contribute to compartmentalization in concert with the differential adhesion dynamics of VE-cadherin caused by turnover to generate long-range position changes of ECs.[46] The present results also indicate that compartmentalized ECs with higher VE-cadherin expression may serve as a scaffold in the axial direction, whereas ECs with lower VE-cadherin expression promote branch elongation through cellular exchange, including tip cell overtaking, with their higher motility. Thus, our study has shed light on the contribution of VE-cadherin to angiogenesis in terms of its effect on cell motility as well as cell adhesion dynamics.

Limitations of the study

This study identified the VE-cadherin-dependent linear and -independent rotational movements as modules of angiogenetic EC behaviors using *in vitro* and *in silico* 2D approaches. However, the validity of this study in *in vivo* 3D angiogenesis could not be tested, although the cell mixing phenomenon has previously been proved in mouse retinal angiogenesis.[9] Moreover, the molecular mechanisms underlying VE-cadherin-dependent asynchrony with asymmetric FA distribution and synchronous rotation in the absence of VE-cadherin remain unsolved.

STAR★METHODS

Detailed methods are provided in the online version of this paper and include the following:

- KEY RESOURCES TABLE
- RESOURCE AVAILABILITY
  - Lead contact
  - Materials availability
  - Data and code availability
- EXPERIMENTAL MODELS AND SUBJECT DETAILS
  - Mice
  - Cell culture
  - Isolation and culture of primary mouse brain endothelial cells (BECs)
  - Ethical considerations
- METHOD DETAILS
  - Matrigel assay
  - Analysis of single-cell behaviors
  - Time-lapse live-cell imaging
  - Cell tracking
  - Analysis of cell trajectories
  - Definitions
  - Generation of VE-cadherin knockout MS-1 cells with the CRISPR/Cas9 method
  - Western blotting
  - Immunofluorescence microscopy
  - Primary antibodies used for western blotting and immunostaining
  - Visualization of F-actin localization and dynamics with live ECs
  - Construction and transfection of plasmids
  - Graphing and statistical analysis
  - Mathematical model
  - Simulation settings

SUPPLEMENTAL INFORMATION

Supplemental information can be found online at https://doi.org/10.1016/j.isci.2023.107051.

AUTHOR CONTRIBUTIONS

K.T. and H.K. conceptualized the project. K.T. designed experiments with useful input from H.K. K.T. performed all experiments. Y. Kurihara contributed to gene-KO experiments. Y.U., T.U., X.L., and H.T. contributed to cell culture experiments. X.L. also contributed to the cell tracking. Y. Kominami contributed to the analysis of cell shape in Figure S5. N.T. contributed to provide the data of the mouse aortic explant assay in Figure S1. Y. Kanai contributed to brain EC experiments. K.T., T.H., M.K., and K.S. performed all data analysis with useful input from Y.U., F.Y., J.M., T.T., and H.K. T.H., F.Y., J.M., and T.T. were contributors for the mathematical modeling and performed the numerical simulations. K.T., T.H., and H.K. wrote the manuscript with useful input from other authors. H.K. supervised the project. K.T. and H.K. acquired fundings for the project. All authors approved the final version of the manuscript to be published.

DECLARATION OF INTERESTS

The authors declare no competing interests.

INCLUSION AND DIVERSITY

We support inclusive, diverse, and equitable conduct of research.

REFERENCES

1. Friedl, P., and Gilmour, D. (2009). Collective cell migration in morphogenesis, regeneration and cancer. Nat. Rev. Mol. Cell Biol. *10*, 445–457. https://doi.org/10.1038/nrm2720.

2. Rørth, P. (2012). Fellow travellers: emergent properties of collective cell migration. EMBO Rep. *13*, 984–991. https://doi.org/10.1038/embor.2012.149.

3. Mayor, R., and Etienne-Manneville, S. (2016). The front and rear of collective cell migration. Nat. Rev. Mol. Cell Biol. *17*, 97–109. https://doi.org/10.1038/nrm.2015.14.

4. Chung, A.S., Lee, J., and Ferrara, N. (2010). Targeting the tumour vasculature: insights from physiological angiogenesis. Nat. Rev. Cancer *10*, 505–514. https://doi.org/10.1038/nrc2868.

5. Kerbel, R.S. (2008). Tumor angiogenesis. N. Engl. J. Med. *358*, 2039–2049. https://doi.org/10.1056/NEJMra0706596.

6. Risau, W. (1997). Mechanisms of angiogenesis. Nature *386*, 671–674. https://doi.org/10.1038/386671a0.

7. Karaman, S., Leppänen, V.M., and Alitalo, K. (2018). Vascular endothelial growth factor signaling in development and disease. Development *145*, dev151019. https://doi.org/10.1242/dev.151019.

8. Hellström, M., Phng, L.K., Hofmann, J.J., Wallgard, E., Coultas, L., Lindblom, P., Alva, J., Nilsson, A.K., Karlsson, L., Gaiano, N., et al. (2007). Dll4 signalling through Notch1 regulates formation of tip cells during angiogenesis. Nature *445*, 776–780. https://doi.org/10.1038/nature05571.

9. Arima, S., Nishiyama, K., Ko, T., Arima, Y., Hakozaki, Y., Sugihara, K., Koseki, H., Uchijima, Y., Kurihara, Y., and Kurihara, H. (2011). Angiogenic morphogenesis driven by dynamic and heterogeneous collective endothelial cell movement. Development *138*, 4763–4776. https://doi.org/10.1242/dev.068023.

10. Jakobsson, L., Franco, C.A., Bentley, K., Collins, R.T., Ponsioen, B., Aspalter, I.M., Rosewell, I., Busse, M., Thurston, G., Medvinsky, A., et al. (2010). Endothelial cells dynamically compete for the tip cell position during angiogenic sprouting. Nat. Cell Biol. *12*, 943–953. https://doi.org/10.1038/ncb2103.

11. Boas, S.E.M., and Merks, R.M.H. (2015). Tip cell overtaking occurs as a side effect of sprouting in computational models of angiogenesis. BMC Syst. Biol. *9*, 86. https://doi.org/10.1186/s12918-015-0230-7.

12. Sugihara, K., Nishiyama, K., Fukuhara, S., Uemura, A., Arima, S., Kobayashi, R., Köhn-Luque, A., Mochizuki, N., Suda, T., Ogawa, H., and Kurihara, H. (2015). Autonomy and non-autonomy of angiogenic cell movements revealed by experiment-driven mathematical modeling. Cell Rep. *13*, 1814–1827. https://doi.org/10.1016/j.celrep.2015.10.051.

13. Mada, J., and Tokihiro, T. (2021). Pattern formation of vascular network in a mathematical model of angiogenesis. Jpn. J. Ind. Appl. Math. *39*, 351–384. https://doi.org/10.1007/s13160-021-00493-9.

14. Matsuya, K., Yura, F., Mada, J., Kurihara, H., and Tokihiro, T. (2016). A discrete mathematical model for angiogenesis. SIAM J. Appl. Math. *76*, 2243–2259. https://doi.org/10.1137/15m1038773.

15. Takubo, N., Yura, F., Naemura, K., Yoshida, R., Tokunaga, T., Tokihiro, T., and Kurihara, H. (2019). Cohesive and anisotropic vascular endothelial cell motility driving angiogenic morphogenesis. Sci. Rep. *9*, 9304. https://doi.org/10.1038/s41598-019-45666-2.

16. Suzuki, S., Sano, K., and Tanihara, H. (1991). Diversity of the cadherin family: evidence for eight new cadherins in nervous tissue. Cell Regul. *2*, 261–270. https://doi.org/10.1091/mbc.2.4.261.

17. Lampugnani, M.G., Resnati, M., Raiteri, M., Pigott, R., Pisacane, A., Houen, G., Ruco, L.P., and Dejana, E. (1992). A novel endothelial-specific membrane protein is a marker of cell-cell contacts. J. Cell Biol. *118*, 1511–1522. https://doi.org/10.1083/jcb.118.6.1511.

18. Tanihara, H., Kido, M., Obata, S., Heimark, R.L., Davidson, M., St John, T., and Suzuki, S. (1994). Characterization of cadherin-4 and cadherin-5 reveals new aspects of cadherins. J. Cell Sci. *107*, 1697–1704. https://doi.org/10.1242/jcs.107.6.1697.

19. Brasch, J., Harrison, O.J., Ahlsen, G., Carnally, S.M., Henderson, R.M., Honig, B., and Shapiro, L. (2011). Structure and binding mechanism of vascular endothelial cadherin: a divergent classical cadherin. J. Mol. Biol. *408*, 57–73. https://doi.org/10.1016/j.jmb.2011.01.031.

20. Giannotta, M., Trani, M., and Dejana, E. (2013). VE-cadherin and endothelial adherens junctions: active guardians of vascular integrity. Dev. Cell *26*, 441–454. https://doi.org/10.1016/j.devcel.2013.08.020.

21. Lagendijk, A.K., and Hogan, B.M. (2015). VE-cadherin in vascular development: a coordinator of cell signaling and tissue morphogenesis. Curr. Top. Dev. Biol. *112*, 325–352. https://doi.org/10.1016/bs.ctdb.2014.11.024.

22. Oda, H., and Takeichi, M. (2011). Structural and functional diversity of cadherin at the adherens junction. J. Cell Biol. *193*, 1137–1146. https://doi.org/10.1083/jcb.201008173.

23. Takeichi, M. (2018). Historical review of the discovery of cadherin, in memory of Tokindo Okada. Dev. Growth Differ. *60*, 3–13. https://doi.org/10.1111/dgd.12416.

24. Scarpa, E., Szabó, A., Bibonne, A., Theveneau, E., Parsons, M., and Mayor, R. (2015). Cadherin switch during EMT in neural crest cells leads to contact inhibition of locomotion via repolarization of forces. Dev. Cell *34*, 421–434. https://doi.org/10.1016/j.devcel.2015.06.012.

25. Arbiser, J.L., Moses, M.A., Fernandez, C.A., Ghiso, N., Cao, Y., Klauber, N., Frank, D., Brownlee, M., Flynn, E., Parangi, S., et al. (1997). Oncogenic H-ras stimulates tumor angiogenesis by two distinct pathways. Proc. Natl. Acad. Sci. USA *94*, 861–866. https://doi.org/10.1073/pnas.94.3.861.

26. Kamei, R., Tanaka, H.Y., Kawano, T., Morii, C., Tanaka, S., Nishihara, H., Iwata, C., and Kano, M.R. (2017). Regulation of endothelial Fas expression as a mechanism of promotion of vascular integrity by mural cells in tumors. Cancer Sci. *108*, 1080–1088. https://doi.org/10.1111/cas.13216.

27. Theveneau, E., and Mayor, R. (2012). Cadherins in collective cell migration of mesenchymal cells. Curr. Opin. Cell Biol. *24*, 677–684. https://doi.org/10.1016/j.ceb.2012.08.002.

28. Masuzzo, P., Van Troys, M., Ampe, C., and Martens, L. (2016). Taking aim at moving targets in computational cell migration. Trends Cell Biol. *26*, 88–110. https://doi.org/10.1016/j.tcb.2015.09.003.

29. Gorelik, R., and Gautreau, A. (2014). Quantitative and unbiased analysis of directional persistence in cell migration. Nat. Protoc. *9*, 1931–1943. https://doi.org/10.1038/nprot.2014.131.

30. Vicsek, T., Czirók, A., Ben-Jacob, E., Cohen, I., and Shochet, O. (1995). Novel type of phase transition in a system of self-driven particles. Phys. Rev. Lett. *75*, 1226–1229. https://doi.org/10.1103/PhysRevLett.75.1226.

31. Li, L., Nørrelykke, S.F., and Cox, E.C. (2008). Persistent cell motion in the absence of external signals: a search strategy for eukaryotic cells. PLoS One *3*, e2093. https://doi.org/10.1371/journal.pone.0002093.

32. Liu, Y.J., Le Berre, M., Lautenschlaeger, F., Maiuri, P., Callan-Jones, A., Heuzé, M., Takaki, T., Voituriez, R., and Piel, M. (2015). Confinement and low adhesion induce fast amoeboid migration of slow mesenchymal

cells. Cell *160*, 659–672. https://doi.org/10.1016/j.cell.2015.01.007.

33. Diao, W., Tong, X., Yang, C., Zhang, F., Bao, C., Chen, H., Liu, L., Li, M., Ye, F., Fan, Q., et al. (2019). Behaviors of glioblastoma cells in in vitro microenvironments. Sci. Rep. *9*, 85. https://doi.org/10.1038/s41598-018-36347-7.

34. Roycroft, A., and Mayor, R. (2016). Molecular basis of contact inhibition of locomotion. Cell. Mol. Life Sci. *73*, 1119–1130. https://doi.org/10.1007/s00018-015-2090-0.

35. Ichikawa, T., Stuckenholz, C., and Davidson, L.A. (2020). Non-junctional role of Cadherin3 in cell migration and contact inhibition of locomotion via domain-dependent, opposing regulation of Rac1. Sci. Rep. *10*, 17326. https://doi.org/10.1038/s41598-020-73862-y.

36. Priya, R., and Yap, A.S. (2015). Making a choice: how cadherin switching controls cell migration. Dev. Cell *34*, 383–384. https://doi.org/10.1016/j.devcel.2015.08.002.

37. Grimsley-Myers, C.M., Isaacson, R.H., Cadwell, C.M., Campos, J., Hernandes, M.S., Myers, K.R., Seo, T., Giang, W., Griendling, K.K., and Kowalczyk, A.P. (2020). VE-cadherin endocytosis controls vascular integrity and patterning during development. J. Cell Biol. *219*, e201909081. https://doi.org/10.1083/jcb.201909081.

38. Hayer, A., Shao, L., Chung, M., Joubert, L.M., Yang, H.W., Tsai, F.C., Bisaria, A., Betzig, E., and Meyer, T. (2016). Engulfed cadherin fingers are polarized junctional structures between collectively migrating endothelial cells. Nat. Cell Biol. *18*, 1311–1323. https://doi.org/10.1038/ncb3438.

39. Riedl, J., Crevenna, A.H., Kessenbrock, K., Yu, J.H., Neukirchen, D., Bista, M., Bradke, F., Jenne, D., Holak, T.A., Werb, Z., et al. (2008). Lifeact: a versatile marker to visualize F-actin. Nat. Methods *5*, 605–607. https://doi.org/10.1038/nmeth.1220.

40. Privratsky, J.R., and Newman, P.J. (2014). PECAM-1: regulator of endothelial junctional integrity. Cell Tissue Res. *355*, 607–619. https://doi.org/10.1007/s00441-013-1779-3.

41. Goodwin, J.M., Svensson, R.U., Lou, H.J., Winslow, M.M., Turk, B.E., and Shaw, R.J. (2014). An AMPK-independent signaling pathway downstream of the LKB1 tumor suppressor controls Snail1 and metastatic potential. Mol. Cell. *55*, 436–450. https://doi.org/10.1016/j.molcel.2014.06.021.

42. Dumbauld, D.W., Michael, K.E., Hanks, S.K., and García, A.J. (2010). Focal adhesion kinase-dependent regulation of adhesive forces involves vinculin recruitment to focal adhesions. Biol. Cell. *102*, 203–213. https://doi.org/10.1042/BC20090104.

43. Katoh, K. (2020). FAK-dependent cell motility and cell elongation. Cells *9*. https://doi.org/10.3390/cells9010192.

44. Nanes, B.A., Chiasson-MacKenzie, C., Lowery, A.M., Ishiyama, N., Faundez, V., Ikura, M., Vincent, P.A., and Kowalczyk, A.P. (2012). p120-catenin binding masks an endocytic signal conserved in classical cadherins. J. Cell Biol. *199*, 365–380. https://doi.org/10.1083/jcb.201205029.

45. Hayashi, T., Yura, F., Mada, J., Kurihara, H., and Tokihiro, T. (2022). Pattern formation of elliptic particles by two-body interactions: a model for dynamics of endothelial cells in angiogenesis. J. Theor. Biol. *555*, 111300. https://doi.org/10.1016/j.jtbi.2022.111300.

46. Bentley, K., Franco, C.A., Philippides, A., Blanco, R., Dierkes, M., Gebala, V., Stanchi, F., Jones, M., Aspalter, I.M., Cagna, G., et al. (2014). The role of differential VE-cadherin dynamics in cell rearrangement during angiogenesis. Nat. Cell Biol. *16*, 309–321. https://doi.org/10.1038/ncb2926.

47. Nakao, S., Platek, A., Hirano, S., and Takeichi, M. (2008). Contact-dependent promotion of cell migration by the OL-protocadherin-Nap1 interaction. J. Cell Biol. *182*, 395–410. https://doi.org/10.1083/jcb.200802069.

48. d'Alessandro, J., Solon, A.P., Hayakawa, Y., Anjard, C., Detcheverry, F., Rieu, J.-P., and Rivière, C. (2017). Contact enhancement of locomotion in spreading cell colonies. Nat. Phys. *13*, 999–1005. https://doi.org/10.1038/nphys4180.

49. Anear, E., and Parish, R.W. (2012). The effects of modifying RhoA and Rac1 activities on heterotypic contact inhibition of locomotion. FEBS Lett. *586*, 1330–1335. https://doi.org/10.1016/j.febslet.2012.03.044.

50. Stramer, B., and Mayor, R. (2017). Mechanisms and in vivo functions of contact inhibition of locomotion. Nat. Rev. Mol. Cell Biol. *18*, 43–55. https://doi.org/10.1038/nrm.2016.118.

51. Carmeliet, P., Lampugnani, M.-G., Moons, L., Breviario, F., Compernolle, V., Bono, F., Balconi, G., Spagnuolo, R., Oosthuyse, B., Dewerchin, M., et al. (1999). Targeted deficiency or cytosolic truncation of the VE-cadherin gene in mice impairs VEGF-mediated endothelial survival and angiogenesis. Cell *98*, 147–157. https://doi.org/10.1016/s0092-8674(00)81010-7.

52. Gory-Fauré, S., Prandini, M.H., Pointu, H., Roullot, V., Pignot-Paintrand, I., Vernet, M., and Huber, P. (1999). Role of vascular endothelial-cadherin in vascular morphogenesis. Development *126*, 2093–2102. https://doi.org/10.1242/dev.126.10.2093.

53. Vittet, D., Buchou, T., Schweitzer, A., Dejana, E., and Huber, P. (1997). Targeted null-mutation in the vascular endothelial-cadherin gene impairs the organization of vascular-like structures in embryoid bodies. Proc. Natl. Acad. Sci. USA *94*, 6273–6278. https://doi.org/10.1073/pnas.94.12.6273.

54. Abraham, S., Yeo, M., Montero-Balaguer, M., Paterson, H., Dejana, E., Marshall, C.J., and Mavria, G. (2009). VE-Cadherin-mediated cell-cell interaction suppresses sprouting via signaling to MLC2 phosphorylation. Curr. Biol. *19*, 668–674. https://doi.org/10.1016/j.cub.2009.02.057.

55. Gaengel, K., Niaudet, C., Hagikura, K., Laviña, B., Muhl, L., Hofmann, J.J., Ebarasi, L., Nyström, S., Rymo, S., Chen, L.L., et al. (2012). The sphingosine-1-phosphate receptor S1PR1 restricts sprouting angiogenesis by regulating the interplay between VE-cadherin and VEGFR2. Dev. Cell *23*, 587–599. https://doi.org/10.1016/j.devcel.2012.08.005.

56. Gavard, J., and Gutkind, J.S. (2006). VEGF controls endothelial-cell permeability by promoting the beta-arrestin-dependent endocytosis of VE-cadherin. Nat. Cell Biol. *8*, 1223–1234. https://doi.org/10.1038/ncb1486.

57. Cao, J., Ehling, M., März, S., Seebach, J., Tarbashevich, K., Sixta, T., Pitulescu, M.E., Werner, A.C., Flach, B., Montanez, E., et al. (2017). Polarized actin and VE-cadherin dynamics regulate junctional remodelling and cell migration during sprouting angiogenesis. Nat. Commun. *8*, 2210. https://doi.org/10.1038/s41467-017-02373-8.

58. Sakurai, T., Woolls, M.J., Jin, S.W., Murakami, M., and Simons, M. (2014). Inter-cellular exchange of cellular components via VE-cadherin-dependent trans-endocytosis. PLoS One *9*, e90736. https://doi.org/10.1371/journal.pone.0090736.

59. Wu, Z., Hofman, F.M., and Zlokovic, B.V. (2003). A simple method for isolation and characterization of mouse brain microvascular endothelial cells. J. Neurosci. Methods *130*, 53–63. https://doi.org/10.1016/s0165-0270(03)00206-1.

60. Coisne, C., Dehouck, L., Faveeuw, C., Delplace, Y., Miller, F., Landry, C., Morissette, C., Fenart, L., Cecchelli, R., Tremblay, P., and Dehouck, B. (2005). Mouse syngenic in vitro blood-brain barrier model: a new tool to examine inflammatory events in cerebral endothelium. Lab. Invest. *85*, 734–746. https://doi.org/10.1038/labinvest.3700281.

61. Hsu, P.D., Scott, D.A., Weinstein, J.A., Ran, F.A., Konermann, S., Agarwala, V., Li, Y., Fine, E.J., Wu, X., Shalem, O., et al. (2013). DNA targeting specificity of RNA-guided Cas9 nucleases. Nat. Biotechnol. *31*, 827–832. https://doi.org/10.1038/nbt.2647.

STAR★METHODS

KEY RESOURCES TABLE

REAGENT or RESOURCE	SOURCE	IDENTIFIER
Antibodies		
Anti-VE Cadherin antibody - Intercellular Junction Marker	Abcam	Cat# ab33168; RRID: AB_870662
Anti-VE Cadherin antibody [EPR18229]	Abcam	Cat# ab205336; RRID: AB_2891001
Purified Rat Anti-Mouse CD144	BD Pharmingen	Cat# 555289; RRID: AB_395707
Purified Rat Anti-Mouse CD31	BD Pharmingen	Cat# 553370; RRID: AB_394816
Anti-Vinculin antibody [EPR8185]	Abcam	Cat# ab129002; RRID: AB_11144129
Donkey Anti-Rabbit IgG H&L (Alexa Fluor® 488)	Abcam	Cat# ab150073; RRID: AB_2636877
Donkey Anti-Rat IgG H&L (Alexa Fluor® 488) preadsorbed	Abcam	Cat# ab150153; RRID: AB_2737355
Donkey Anti-Rat IgG H&L (Alexa Fluor® 555) preadsorbed	Abcam	Cat# ab150154; RRID: AB_2813834
Polyclonal Swine Anti-Rabbit Immunoglobulins/HRP	Dako	Cat# P0399; RRID: AB_2617141
Chemicals, peptides, and recombinant proteins		
Cellmatrix Type I-A	Nitta Gelatin	N/A
SYTO16	Invitrogen	S7578
Hoechst 33342	Dojindo Laboratories	H342
EGM™-2 Endothelial Cell Growth Medium-2 Bullet Kit™	Lonza	CC-3162
Dextran 60,000	FUJIFILM Wako Pure Chemical Corporation	047-30522
Collagenase/disperse	Roche Diagnostics	10269638001
DNaseI	Sigma-Aldrich	11284932001
Tosyl-L-lysyl-chloromethane hydrochloride	FUJIFILM Wako Pure Chemical Corporation	200-20141
Puromycine	FUJIFILM Wako Pure Chemical Corporation	160-23151
Endothelial Cell Basal Medium 2	Takara Bio inc.	C-22011
Cellmatrix Type I-C	Nitta Gelatin	N/A
Endothelial cell growth supplement from bovine neural tissue	Sigma-Aldrich	E2759
Protease Inhibitor Cocktail	Sigma-Aldrich	P8340
Ponceau S stain solution	Muto pure chemicals	N/A
4′,6-Diamidino-2-phenylindole Dihydrochloride	Sigma-Aldrich	D9542
Acti-stain™ 555 phalloidin	Cytoskeleton	PHDH1
Lipofectamine™ 3000 Transfection Reagent	Thermo Fisher Scientific	L3000008
Trypsin-EDTA	Nacalai Tesque	32777-15
M-MLV-Reverse Transcriptase	NIPPON GENE CO., LTD.	28025013
Ex taq Version 2.0	Takara Bio inc.	RR003A
*Sac*II restriction endonuclease	NIPPON GENE CO., LTD.	319-00922
*Xma*I restriction endonuclease	New England Biolabs.	R0180S
Pfx50™ DNA Polymerase	Invitrogen	12355-012
Critical commercial assays		
Endothelial Tube Formation Assay	Cell Biolabs	CBA-200
DC™ Protein Assay Kit I	BioRad	#5000111
Amersham ECL Select Western Blotting Detection Reagent	Amersham Bioscience	RPN2235

(Continued on next page)

Continued

REAGENT or RESOURCE	SOURCE	IDENTIFIER
Takara DNA Ligation Kit	Takara Bio inc.	6023
Deposited data		
Source data	This study	https://doi.org/10.6084/m9.figshare.21952793
Raw data (coordinates of the cells)	This study	https://doi.org/10.6084/m9.figshare.21952727
Customized scripts and usage instructions	This study	https://github.com/RoastedGreenTeaaa/scripts-angiogenesis
Experimental models: Cell lines		
MS-1	ATCC	CRL-2279
NIH3T3	ATCC	CRL-1658
10T 1/2	ATCC	CCL-226
MDCK.2	ATCC	CRL-2936
Vero	ATCC	CCL-81
COS7	ATCC	CRL-1651
BAEC (Bovine Aortic Endothelial Cells)	Cell Applications	B304-05
HUVEC (C2519)	Lonza	C2519A
HUVEC (03331)	Lifeline Cell Technology	FC-0003
Primary Mouse Brain Endothelial Cells	This study	N/A
VE-cadherin knockout MS-1 cells	This study	N/A
Experimental models: Organisms/strains		
C57BL/6J mice	CLEA Japan Inc.	https://www.clea-japan.com/en/
Oligonucleotides		
CRISPR/Cas9 targeting sequence: the VE-cadherin #1: 5'-AGCATTCTGGCGGTTCACGT-3'	This study	N/A
CRISPR/Cas9 targeting sequence: the VE-cadherin #2: 5'-TGAATCGCTGCCCCACTATG-3'	This study	N/A
Primer sequence: VE-cadherin open reading frame #1: 5'-AAACCGCGGGAAGGATGCAGAGGCTCACA-3'	This study	N/A
Primer sequence: VE-cadherin open reading frame #2: 5'-TTTCCCGGGATGATGAGTTCCTCCTGGGG-3'	This study	N/A
Primer sequence: VE-cadherin-DEEmut #1: 5'-GGTCACTTACGCTGCGGCGGGCGGTGGTGAG-3'	This study	N/A
Primer sequence: VE-cadherin-DEEmut #2: 5'-CTCACCACCGCCCGCCGCAGCGTAAGTGACC-3'	This study	N/A
Recombinant DNA		
Plasmid: Plasmid pCMVLifeAct-TagRFP	ibidi GmbH	60102
pX330 CRISPR/Cas9 plasmid	Addgene	#42230
pTAC2-pgk-Puro1 plasmid	This study	N/A
pTAC-2 vector	Biodynamics Laboratory	DS126
pTAKN-2 vector	Biodynamics Laboratory	DS130
pEGFP-N3 vector	Clontech	6080-1
VE-cadherin-EGFP vector	This study	N/A
VE-cadherin-DEEmut-EGFP vector	This study	N/A

(Continued on next page)

Continued

REAGENT or RESOURCE	SOURCE	IDENTIFIER
Software and algorithms		
Image-Pro Premier 3D Version 9.2 software	Media Cybernetics	https://www.mediacy.com/
Image J software (ImageJ 1.52a)	National Institutes of Health	https://imagej.nih.gov/ij/download.html
Microsoft excel software	Microsoft	N/A
GraphPad Prism9	GraphPad Software	N/A
The CRISPR design web site	Feng Zhang Lab	http://crispr.mit.edu/
Fortran 90		N/A
Mathematica 13.1	Wolfram Research, Inc.	N/A
Other		
3.5 cm glass-bottomed dish	Matsunami Glass	D11130H
3.5 cm collagen-coated glass-bottom dish	Matsunami Glass	D11134H
All-in-One Fluorescence Microscope BZ-X710	Keyence	N/A
FV-10i confocal laser scanning microscope	Olympus	N/A
Immobilon-P PVDF membrane	Millipore	IPVH00010
ImageQuant LAS 4000 mini	GE Healthcare Japan	N/A

RESOURCE AVAILABILITY

Lead contact

Further information and requests for resources and reagents should be directed to, and will be fulfilled, by the lead contacts, Hiroki Kurihara (kuri-tky@umin.net).

Materials availability

Cell lines generated in this study will be made available upon request to the lead contact.

Data and code availability

- All source data (original western blot images) and raw data (coordinates of the cells) that support the findings of this study are available in Figshare. DOIs are listed in the key resources table. Customized scripts and usage instructions are available from Github: https://github.com/RoastedGreenTeaaa/scripts-angiogenesis.

- This paper does not report original code.

- Any additional information required to reanalyze the data reported in this paper is available from the lead contact upon request.

EXPERIMENTAL MODELS AND SUBJECT DETAILS

Mice

C57BL/6J mice were purchased from CLEA Japan Inc. (Tokyo, Japan). Two to five individuals were housed per cage in SPF conditions in an environmentally controlled room at 23°C±2°C, with a relative humidity of 50%–60% and under a 12-hour light/dark cycle.

Cell culture

MS-1 cells (mouse pancreatic islet-derived endothelial, transformed by SV40 large T antigen), NIH3T3 cells and 10T 1/2 cells (mouse embryonic fibroblasts), MDCK cells (canine, kidney, epithelial), Vero cells (African green monkey, kidney, epithelial), COS7 cells (African green monkey, kidney, epithelial, transformed), and BAECs (bovine aortic endothelial) were cultured in high-glucose DMEM (FUJIFILM Wako Pure Chemical Corporation, Japan) containing 10% fetal bovine serum (Sigma) and antibiotics (penicillin and strepto-mycin, Nacalai Tesque, Japan). HUVECs (Human umbilical vein endothelial cells) were cultured in EGM^{TM}-2 Endothelial Cell Growth Medium-2 Bullet Kit^{TM} (Lonza). All cells were cultivated at 37°C in a hu-midified atmosphere containing 5% CO_2 and passaged before cells reached 80% confluence. All cells were

washed with phosphate-buffered saline (PBS) and dissociated with Trypsin-EDTA (Nacalai Tesque, Japan). All cell lines had been tested for mycoplasma contamination.

Isolation and culture of primary mouse brain endothelial cells (BECs)

The primary culture of BECs was performed in accordance with a previously described method[59,60] with some modifications. Brains were aseptically collected from 4–8-week-old C57BL/6J mice (5 males and 5 females) and disrupted in Hanks' Balanced Salt Solution (HBSS; FUJIFILM Wako Pure Chemical Corporation, Japan) using a Dounce homogenizer. The homogenates were suspended in 18% dextran (FUJIFILM Wako Pure Chemical Corporation, Japan) in MEM-HAF (MEM with 25 mM HEPES/AA/2% FBS, FUJIFILM Wako Pure Chemical Corporation, Japan) and centrifuged at 4,000rpm for 20 min. Packed myelin and the upper phase over the microvessels (MVs) layer were removed. The MVs layer was collected with 10 mL MEM-HAF and centrifuged at 100 g for 10 min. The pellet was digested in collagenase/disperse (2 mg/mL; Roche Diagnostics) in MEM-HAF (FCS-free) supplemented with 10 μg/mL DNase I (Sigma) and 0.294 μg/mL tosyl-L-lysyl-chloromethane hydrochloride (FUJIFILM Wako Pure Chemical Corporation, Japan) for 30 min at 37°C in a shaking water bath. The digested microvessels were washed and collected with F12 (Sigma) containing 10% FCS and centrifuged twice at 300 g for 5 minutes. Isolated BECs were seeded with endothelial cell growth medium (ECGM) composed of Endothelial Cell Basal Medium 2 (Takara Bio inc., Japan) and Endothelial cell growth supplement from bovine neural tissue (Sigma) in a 3.5 cm glass-bottomed dish (Matsunami Glass, Japan, D11130H) coated with collagen type I-C (Nitta Gelatin, Osaka, Japan) and cultured with 4 μg/mL puromycin in ECGM. The isolation of BECs was checked using PECAM1 protein expression.

Ethical considerations

Animal experiments were performed in accordance with the guidelines of the University of Tokyo Animal Care and Use Committee with approval from the institutional review board (approval number; M-P19-050). All experiments conform to relevant regulatory standards.

METHOD DETAILS

Matrigel assay

To prepare Matrigel, 10 μL of extracellular matrix (ECM) solution packaged in the Endothelial Tube Formation Assay Kit (Cell Biolabs) was solidified on a 1.4 cm glass bottom in a 3.5 cm glass-bottomed dish (Matsunami Glass, Japan, D11130H) by 30min incubation at 37°C. Cells were resuspended in DMEM containing 10% FCS after dissociation with trypsin-EDTA (Nacalai Tesque, Japan) and 6.0×10^4 cells were seeded around the solidified Matrigel on the glass-bottomed area of the dish. When cells were attached to the dish bottom (6–8 hours after seeding), complete DMEM was supplied to fill the 3.5 cm dish. Cells were viewed using a fluorescence microscope (BZ-X710; Keyence, Japan) and time-lapse images were recorded with a confocal laser scanning microscope (FV-10i confocal laser scanning microscope; Olympus) at 5-minute intervals. See also Figure S1 and "Time-lapse live-cell imaging".

Analysis of single-cell behaviors

Before the cells to be analyzed were seeded, the same cells were seeded at a high density (2.5×10^5 cells or 3.0×10^4 cells/cm^2) on the plastic space around the glass bottom region to supply cell-secreted growth factors. The plastic space was pre-coated with collagen (Cellmatrix Type I-A; Nitta Gelatin, Osaka, Japan) to allow cells to attach. For the analysis of single-cell behaviors, analyzed cells were seeded at a low density (1.0–5.0×10^3 cells or 1.0–5.0×10^2 cells/cm^2) on the 3.5 cm collagen-coated glass-bottom dish (Matsunami Glass, Japan, D11134H) to keep sufficient distance between the cells so that one- and two-cells were captured in a field. After incubation at 37°C overnight, time-lapse live-cell imaging was performed following cell tracking. See "Time-lapse live-cell imaging" and "Cell tracking".

Time-lapse live-cell imaging

Time-lapse fluorescence and phase-contrast images were acquired every 5-minutes using a confocal laser scanning microscope (FV-10i confocal laser scanning microscope; Olympus) with a 10 × 0.4 NA air objective lens for the single-cell analysis and Matrigel assay. LifeAct-RFP images were captured at 2-minute intervals with a 60 × 1.2 NA water-immersion objective lens. Laser wavelengths of 405 nm, 473 nm and 559 nm were used for the acquisition of the images for SYTO16, Hoechst 33342, and RFP signals, respectively. The microscope was equipped with an on-stage incubation chamber that maintained the

temperature at 37°C and the CO_2 concentration at 5%. Cell nuclei were labeled with SYTO16 (100 nM, Invitrogen) for EC lines and Hoechst 33342 (200 ng/mL, Dojindo Laboratories, Japan) for other cell lines. Before experiments were performed, unattached cells and floating cells were removed by extensive washing with complete medium and the attached cells' nuclei were stained in complete medium containing SYTO16 or Hoechst 33342. Hoechst 33342 was washed from the culture medium after incubation for 1 hour at 37°C.

Cell tracking

Individual cell paths were automatically or manually tracked from fluorescence images of cell nuclei stained by SYTO16 or Hoechst 33342 staining and converted to *xy* coordinates using Image-Pro Premier 3D Version 9.2 software (Media Cybernetics). Signals for the nuclei were sharpened and segmented with 2D filters available in Image-Pro Premier software. The coordinates of the nuclei were defined as the center of mass of the refined nuclei signals. For cell tracking in the Matrigel assay, all cells were tracked manually by visual inspection. In the single-cell analysis, we used the automatic cell tracking function of Image-Pro Premier; however, we performed manual tracking when the nuclei signals were indistinguishable using automatic tracking.

Analysis of cell trajectories

For the analysis of cell motility at a single-cell level, cell trajectories were recorded consecutively for the 1-cell and 2-cell states, respectively. In all cell trajectories, the periods 2 hours before and after the onset of anaphase were excluded from the analysis to avoid the influence of cell division on cell motility. For the 2-cell analysis, the trajectories of paired 2-cells derived from 1 cell after cell divisions were analyzed from 2 hours after the onset of anaphase.

Individual cell trajectories were smoothened using a simple moving average (SMA; $SMA = \frac{A_1 + A_2 + ... + A_n}{n}$, n = the total number of frames of a selected range) filter. The filtering of cell trajectories with 5-frame SMA was used in the analysis of cell migrations. One frame corresponds to 5 minutes in the time-lapse images of MS-1 cells and 3 minutes in the mouse aortic explant assay, respectively. Note that non-smoothened trajectories were used in the calculation of instantaneous speed and spatial distance in Figures 1H, and S1I.

To quantify the differences in migration behaviors, smoothened trajectories of individual cells were analyzed in terms of migration speed, mean square displacement (MSD), directionality ratio (DR), and order parameter (OP). The MSD was calculated as the average squared displacement in a migration trajectory over increasing time intervals.[29] The MSD is a value for the surface area explored by the cell over time containing information about the persistence of cell migration. The slope of these log–log plots is a useful index for directional persistence: it is equal to 1 for randomly moving cells and to 2 for cells that move in a perfectly straight manner. The DR is a parameter that quantifies the trajectory straightness; it is also known as the confinement ratio, persistence ratio, meandering index, or straightness index. The DR was obtained by dividing the displacement by the trajectory length at time t[29]. The DR is equal to 1 for a fully straight trajectory and equal to 0 for a fully curved trajectory. The OP is used for the analysis of direction autocorrelation. Displacement vectors describing migration trajectory are normalized to the same length, and vector angles are compared pairwise over time. When the velocities of all observed cells were aligned, OP is equal to 1, and when the alignment of velocities was lost, it became smaller. Data analysis was executed in Mathematica 13.1 (Wolfram Research, Inc., Champaign, US).

Definitions

The term "tip cells" refers to "cells at the tip of a certain time point." The other cells are termed "stalk cells". "Passing" refers to "cells passing each other within a 20 μm distance changing the sign of relative position along the direction of elongation." In the comparative analysis of cell speed, "Passing" cells include cells undergoing "passing each other" within 25 minutes (angiogenic sprouting of MS-1 cells), 30 minutes (mouse aortic explant assay), or 25 steps (mathematical model). The others are referred to as "Not passing." In the analysis of instantaneous speed at the time of "Passing," "Total," "Forward," and "Backward" indicates the direction of cell movement. "Distance" indicates the distance between the center of the nuclei of two cells passing each other. Time 0 is considered the moment when the two cells pass each other. The trajectory analysis of ECs in angiogenic sprouting was performed by projecting nuclear positions orthogonally onto the axis of branch elongation.[9,15] The axis of elongation was set by drawing a line

connecting the start and end points of the tip position. For tip cell parameters, "elongation drive" (elongation of a branch)/(number of tip cells during the total observed time) and "tip duration" (overall time)/ (number of tip cells during the total observed time) were introduced as described previously.[9] For the 2-cell analysis, "rotational movement" was defined as the movement keeping the relative velocity angle within 120°–180° for more than 1 hour.

Generation of VE-cadherin knockout MS-1 cells with the CRISPR/Cas9 method

Guide RNA sequences for CRISPR/Cas9 were designed using the CRISPR design web site (http://crispr.mit. edu/) provided by the Feng Zhang Lab.[61] Two sets of single-guide RNAs were generated to target the coding region of the mouse VE-cadherin gene *Cdh5* as follows: #1: 5′-AGCATTCTGGCGGTTCACGT-3′/ 5′-ACGTGAACCGCCAGAATGCT-3′, #2: 5′-TGAATCGCTGCCCCACTATG-3′/5′-CATAGTGGGGCAGC GATTCA-3′. The complementary oligonucleotides for guide RNAs (gRNAs) were annealed and cloned into pX330 CRISPR/Cas9 plasmid (Addgene). MS-1 cells were co-transfected with either pX330/sgRNA#1 or pX330/sgRNA#2, and pTAC2-pgk-Puro1 plasmid, which contains the puromycin resistance gene downstream to the PGK-promoter in the pTAC-2 vector (Biodynamics Laboratory), using Lipofectamine 3000 (Life Technologies). On the second day after transfection, the cells were treated with 2–4 μg/mL of puromycin (FUJIFILM Wako Pure Chemical Corporation, Japan) for 3 days. After 2 weeks, the colonies were isolated with the cloning cylinders. VE-cadherin knockout was confirmed by DNA sequencing and western blotting analysis.

Western blotting

To prepare protein lysates, the cells were solubilized in PBS containing 1% Triton X-100, 0.1% sodium deoxycholate, 0.02% sodium dodecyl sulfate (SDS), 1 mM phenylmethylsulfonyl fluoride, 0.5 mM vanadate, and protease inhibitor cocktail (Sigma). After three 10-second periods of sonication, the samples were subjected to protein analysis. The protein concentration was determined using a DC™ Protein Assay Kit I (BioRad), and samples containing equal amounts of protein were separated by 7.5% SDS–polyacrylamide gel electrophoresis (PAGE) and then electrotransferred to a polyvinylidene difluoride (PVDF) membrane (Immobilon-P; Millipore). The membrane was stained with Ponceau S stain solution (Muto pure chemicals, Japan) to assess transfer quality and estimate the total protein content, and then washed for 5 minutes in TBST (0.1% Tween 20 in Tris-buffered saline, pH 7.6) to remove Ponceau staining. After non-specific binding was blocked by incubation in blocking solution (5% skim milk in TBST) for 1 hour at room temperature (RT), the blot was probed with primary antibody diluted in blocking solution overnight at 4°C. The membrane was then washed three times for 5 minutes with TBST at RT, incubated with secondary antibody (polyclonal swine anti-rabbit immunoglobulins/HRP, Dako) in blocking solution for 1–2 hours at RT, and washed four times for 10 minutes with TBST at RT. The signals were detected using the ECL chemiluminescence detection system (Amersham Bioscience) and imaged with ImageQuant LAS 4000 mini (GE Healthcare Japan).

Immunofluorescence microscopy

Cells were fixed with 4% paraformaldehyde in PBS for 10 minutes at RT, permeabilized with 0.2% Triton X-100 in PBS, and washed three times for 5 minutes with PBS at RT. After non-specific binding was blocked by incubation with blocking solution (10% goat serum or 3% bovine serum albumin in PBS), the cells were incubated with the primary antibodies diluted in blocking solution overnight at 4°C. Then, the cells were washed and stained with the secondary antibodies (donkey anti-rabbit or anti-rat IgG H&L Alexa Fluor® 488 or donkey anti-rat IgG H&L Alexa Fluor® 555, Abcam) in blocking solution for 1–2 hours at RT. For cell nuclei and actin staining, Acti-stain™ 555 fluorescent phalloidin (cytoskeleton, PHDH1) and DAPI (4′,6-diamidino-2-phenylindole dihydrochloride; Sigma) were added to the reaction buffer containing the secondary antibody. After three washes for 10 minutes in PBS at RT, the cells were viewed using a fluorescence microscope (BZ-X710; Keyence, Japan). Signal intensities were analyzed using ImageJ software (ImageJ 1.52a, National Institutes of Health).

Primary antibodies used for western blotting and immunostaining

The primary antibody used for western blotting was rabbit monoclonal anti-VE-cadherin antibody (Abcam, ab33168), 2.0 μg/mL. The primary antibodies used for immunostaining were rabbit monoclonal anti-VE-cadherin antibody (Abcam, ab205336), 2.38 μg/mL; purified rat anti-mouse CD144 (BD Pharmingen,

555289), 5.0 μg/mL; purified rat anti-mouse CD31 [PECAM1] (BD Pharmingen, 553370), 5.0 μg/mL; and rabbit monoclonal anti-vinculin antibody [EPR8185] (Abcam, ab129002), 10.8 μg/mL.

Visualization of F-actin localization and dynamics with live ECs

We visualized F-actin organization and dynamics with LifeAct-RFP. Plasmid p^{CMV}LifeAct-TagRFP (ibidi GmbH) was transfected into wild-type and VE-cadherin-KO MS-1 cells with Lipofectamine 3000 (Life Technologies) in accordance with the manufacturer's protocol. At 24–48 hours after transfection, the transfected cells were dissociated with trypsin-EDTA (Nacalai Tesque, Japan) and seeded onto the collagen-coated glass coverslip bottom dish (Matsunami Glass, Japan, D11134H) to keep sufficient distance between cells so that interactive behaviors in a two-cell state after cell division were captured. After incubation at 37°C overnight, time-lapse live-cell imaging was performed at 3-minute intervals.

Construction and transfection of plasmids

For the expression of VE-cadherin-enhanced green fluorescent protein (EGFP) fusion protein, the VE-cadherin open reading frame was amplified by reverse transcription (RT)-PCR from MS-1 cell cDNA samples using M-MLV-Reverse Transcriptase (NIPPON GENE CO., LTD., Japan) and Ex taq Version 2.0 (Takara Bio inc., Japan), and then subcloned in frame into the pEGFP-N3 vector (GenBank Accession#: U57609; Addgene) with Takara DNA Ligation Kit (Takara DNA Ligation Kit) using the SacII and XmaI restriction enzyme sites. For the construction of the endocytosis-defective VE-cadherin mutant (VE-cadherin-DEEmut-EGFP), PCR-based site-directed mutagenesis was used to mutate the region of 646–648 amino acid sequence (DEE→AAA). VE-cadherin-DEEmut sequence was amplified by RT-PCR from VE-cadherin-EGFP vector using Pfx50™ DNA Polymerase (Invitrogen) with complementary nucleotide primer pairs specifically converting 5′-gatgaggag-3′ into 5′-gctgcggcg-3′. Nucleotide sequences used for vector construction were listed in the key resource table. All constructs were verified by sequencing and transfected with Lipofectamine 3000 reagent (Life Technologies) according to the manufacturer's protocol. Cells transfected with plasmids encoding EGFP derivatives were observed by fluorescence microscopy 24 hours after transfection.

Graphing and statistical analysis

Microsoft Excel software or GraphPad Prism 9 (GraphPad Software) were used for graph construction. All statistical analysis was performed using GraphPad Prism 9 or Microsoft Excel software. All errors presented in the text are the SEM for quantitative values or error margin for percentages. Comparisons of two groups of paired data were performed using a paired *t*-test. The comparison of two groups of independent data were performed using Welch's *t*-tests or the Mann–Whitney U test. Pairwise multiple comparisons were performed using one-way ANOVA and Dunn's test or Dunnett's test, or Kruskal-Wallis test and Dunn's test. The Shapiro–Wilk test was used to check for normal distribution. Statistical significance was denoted by *P <0.05, **P <0.01, ***P <0.001, and **** P <0.0001. ns, not significant. Sample number of each plot can be found in the figure legends.

Mathematical model

Our previous elliptic particle model based on Newtonian dynamics[45] was adopted with some modifications. In this model, the cells were approximated as elliptic particles with a and b for the semi-major and semi-minor axes, respectively. A parametric equation of the i-th endothelial cell (hereafter called "EC-i") is

$$\begin{pmatrix} x(\theta) \\ y(\theta) \end{pmatrix} = r_i + \begin{pmatrix} \cos \psi_i & -\sin \psi_i \\ \sin \psi_i & \cos \psi_i \end{pmatrix} \begin{pmatrix} a & 0 \\ 0 & b \end{pmatrix} \begin{pmatrix} \cos \theta \\ \sin \theta \end{pmatrix}$$

(Equation 1)

where $\theta \in [0, 2\pi)$ is a parameter, $r_i \in \mathbb{R}^2$ is the center of an ellipse, and $\psi_i \in [-\pi/2, \pi/2)$ is the orientation angle (Figure S5A). For $S \in \mathbb{Z}_{>0}$ and $\theta_k := 2\pi k/S$, we set S sampling points on the ellipse boundary as $(x(\theta_k), y(\theta_k))$ $(k = 0,1,...,S - 1)$. In the present study, each cell is represented as two concentric ellipses, in which the outer ellipse $(a = a_1, b = b_1)$ denotes the region of the attractive force, whereas the inner one $(a = a_2, b = b_2)$ denotes the region of the repulsive force (Figures S5A–S5C). We regard that EC-i and EC-j are in contact with each other when any of sampling points on the ellipse of EC-i are located inside the ellipse of EC-j. Here, we adopted $S = 16$ through numerical simulations using several values of S; this did not significantly affect our results. The state of EC-i at time t is characterized by its position $r_i \in \mathbb{R}^2$, velocity $v_i \in \mathbb{R}^2$, and the direction of the long axis $\psi_i \in [-\pi/2, \pi/2)$ (Figures S5A–S5H). In this study, we include the

phase $\phi_i \in [-\pi, \pi)$ as a parameter to reflect the different synchronicity of wild-type and VE-cadherin-KO cells (Figure S5F and S5G). We consider the following discrete equations for the dynamics of ECs.

$$r_i^{t+1} = r_i^t + v_i^t \qquad \text{(Equation 2a)}$$

$$v_i^{t+1} = v_i^t - \gamma(\phi_i^t) M(\phi_i^t)^{-1} v_i^t + M(\phi_i^t)^{-1} \left(\sum_{j \neq i} F_{i,j}{}^t + D_i{}^t \right) \qquad \text{(Equation 2b)}$$

$$\psi_i^{t+1} \equiv \psi_i^t - \gamma_1 \sin(2(\psi_i^t - q(v_i^{t+1}))) \pmod{\pi} \qquad \text{(Equation 3)}$$

$$\phi_i^{t+1} \equiv \phi_i^t - \gamma_2 \sin\phi_i^t + \sum_{j \neq i} \Lambda_{i,j}{}^t (\mu \sin(\phi_i^t - \phi_j^t) + \omega_0 + \xi_i) \pmod{2\pi} \qquad \text{(Equation 4)}$$

Equations 2a and 2b are the discretized Newtonian equations of motion. Here, $M(\phi_i^t)$ is the mass of an EC and $\gamma(\phi_i^t)$ is a damping parameter, and we assumed that $M(\phi_i^t)$ and $\gamma(\phi_i^t)$ depend on the phase ϕ_i^t. Using a step function $U(x) := 1 \, (x \geq 0), 0 \, (x < 0)$, we set $M(\phi_i^t)^{-1} = U(\sin\phi_i^t + \varepsilon)$ and $\gamma(\phi_i^t) M(\phi_i^t)^{-1} = \gamma_0 + (1 - \gamma_0)(1 - U(\sin\phi_i^t + \varepsilon))$, where ε and γ_0 are positive constants. For the interaction, $F_{i,j}{}^t$ denotes the two-body interaction between ECs and $\Sigma_{j \neq i}$ denotes the summation over all the ECs connected with the EC-i in the region of attraction. For the force on the EC-i, we adopt the following (Figures S5B and S5C):

(a) If there is no overlap between the two ECs, then $F_{i,j}{}^t = 0$

(b) If there is overlap between the two attractive ellipses, but no overlap between the two repulsive ellipses, then $F_{i,j}{}^t = -f_a e_{i,j}{}^t$

(c) If there is overlap between the two repulsive ellipses, then $F_{i,j}{}^t = f_r e_{i,j}{}^t$

Here, $e_{i,j}{}^t := (r_i^t - r_j^t)/\|r_i^t - r_j^t\|$ and f_r, f_a are the positive constants for the strengths of interaction. Note that the collision of two ellipses is determined from whether sampling points on the ellipse is included in the other ellipse, as described above. The final term D_i^t, denotes the self-driving force, which reflects the potentiation of locomotion caused by cell-to-cell contact (Figure S5D). If the EC-i comes into contact with other ECs, then $D_i{}^t = dv_i^t/\|v_i^t\|$, where the parameter d is a positive constant. If there is no interaction between the two ECs or $\|v_i^t\| = 0$, then $D_i{}^t = 0$.

Equation 3 means that an EC rotates with its long axis oriented in the moving direction; γ_1 is a positive constant and $q(v)$ denotes the angle between the velocity v and the horizontal axis (Figure S5E). Note that if the EC-i stops ($\|v_i^{t+1}\| = 0$), then $\psi_i^{t+1} = \psi_i^t$.

Equation 4 is the internal variable that represents the anti-phase synchronization when paired ECs come into contact with each other, in which we assume that phases of isolated ECs or VE-cadherin-KO cells are zero. For the parameters in Equation 4, γ_2 is a positive constant, μ is a coupling constant, ω_0 is an angular velocity, ξ_i is a noise term, $\Lambda_{i,j}{}^t \in \{0, 1\}$ is a parameter that indicates whether EC-i and EC-j interact with each other through VE-cadherin; $\Lambda_{i,j}{}^t = 1$ if the two ECs have VE-cadherin and there is the overlap in the attraction regions between two ellipses, otherwise $\Lambda_{i,j}{}^t = 0$.

We explain the relationship between the equation of motion (2b) and the phase Equation 4. Let us consider interacting ECs because an EC without cell–cell interaction with others stops in our model. For two ECs with VE-cadherin (wild-type ECs), they mutually migrate or stop (Figure S5F). As $U(\sin\phi_i^t + \varepsilon) = 1$ when $\sin\phi_i^t + \varepsilon \geq 0$, we have:

$$M(\phi_i^t)^{-1} = U(\sin\phi_i^t + \varepsilon) = 1$$

$$\gamma(\phi_i^t) M(\phi_i^t)^{-1} = \gamma_0 + (1 - \gamma_0)(1 - U(\sin\phi_i^t + \varepsilon)) = \gamma_0.$$

Hence, Equation 2b gives:

$$v_i^{t+1} = v_i^t - \gamma(\phi_i^t) M(\phi_i^t)^{-1} v_i^t + M(\phi_i^t)^{-1} \left(\sum_{j \neq i} F_{i,j}{}^t + D_i{}^t \right)$$

$$= v_i^t - \gamma_0 v_i^t + \sum_{j \neq i} F_{i,j}^t + D_i^t \qquad \text{(Equation 5)}$$

Similarly, as $U(\sin \phi_i^t + \varepsilon) = 0$ when $\sin \phi_i^t + \varepsilon < 0$, we have

$$M(\phi_i^t)^{-1} = U(\sin \phi_i^t + \varepsilon) = 0,$$

$$\gamma(\phi_i^t) M(\phi_i^t)^{-1} = \gamma_0 + (1 - \gamma_0)(1 - U(\sin \phi_i^t + \varepsilon)) = 1$$

Hence, Equation 2b gives

$$v_i^{t+1} = v_i^t - \gamma(\phi_i^t) M(\phi_i^t)^{-1} v_i^t + M(\phi_i^t)^{-1} \left(\sum_{j \neq i} F_{i,j}^t + D_i^t \right) = v_i^t - v_i^t + 0 = 0.$$

Therefore, the two ECs reciprocally switch between locomotion and pause. For VE-cadherin-KO cells, their phases become zero and their motion follows Equation 5 (Figure S5G). Since $\Lambda_{i,j}^t = 0$ for VE-cadherin-KO cells, Equation 4 gives:

$$\phi_i^{t+1} \equiv \phi_i^t - \gamma_2 \sin \phi_i^t + \sum_{j \neq i} \Lambda_{i,j}^t \left(\mu \sin(\phi_i^t - \phi_j^t) + \omega_0 + \xi_i \right) = \phi_i^t - \gamma_2 \sin \phi_i^t.$$

The phase ϕ_i^t approaches zero because γ_2 is a positive constant. If $\phi_i^t = 0$, $U(\sin \phi_i^t + \varepsilon) = U(\varepsilon) = 1$. Thus, VE-cadherin-KO cells move according to Equation 5.

Simulation settings

The common parameters for the simulation of wild-type and VE-cadherin-KO MS-1 ECs are $a_1 = 30$, $b_1 = 20$, $a_2 = 20$, $b_2 = 5$, $f_a = 0.005$, $f_r = 0.075$, $\gamma_0 = 0.05$, $d = 0.005$, $\varepsilon = 0.15$, and $\gamma_2 = 0.01$. Here the unit of length is supposed to be microns. For the parameters γ_1, μ and ω_0, we used $\gamma_1 = 0.005$, $\mu = 0.3$, and $\omega_0 = 0.01$ for wild-type cells and $\gamma_1 = 0.02$ and 0.05, $\mu = 0.0$, $\omega_0 = 0.0$ for VE-cadherin- KO cells. The parameters for the ellipticity (a_1, b_1, a_2, b_2) were estimated from the shape analysis of ECs and the distance between ECs. Then, χ was the flattening of an ellipse defined by

$\chi = 1 - b/a$, where a and b are the semi-major and semi-minor axes, respectively. We extracted the contours of 28 ECs from the transmission image and obtained the flattening of each cell with ImageJ (NIH). In our simulation, we adopted $\chi = 0.75$, which was the median of the dataset shown in Figure S5I. We determined (a_1, b_1, a_2, b_2) from the flattening $\chi = 0.75$ and the typical result of cell-to-cell distance. The minor axis $2b_2$ was assumed to be 10 because the minimum distance between two ECs was approximately 10 μm. From $\chi = 1 - b_2/a_2$, we obtained $a_2 = 20$. Usually, two ECs come into contact with each other while maintaining the orientation of their long axes (Figure S5H). We assumed that the distance along the minor axes of two ECs was the average distance ($\sim$40 μm), and set $b_1 = 20$. Considering the maximum distance ($\sim$60 μm), we set $a_1 = 30$. We used the strengths of attraction and repulsion, f_a and f_r, respectively, as estimated previously.[15] We set the parameters for the phase equation $(\gamma_2, \mu, \omega_0, \varepsilon)$ from observations of the presumptive cycle, in which a pair of wild-type cells seem to switch between locomotion and pause (200–300 minutes). The parameters γ_0, d and γ_1 were determined by observing the movies of time-lapse imaging datasets. This observation suggests that a pair of wild-type cells tends to maintain the orientation of its long axis. In contrast, a pair of VE-cadherin-KO cells tend to change their direction quickly.

In simulations of the dynamics of a pair of ECs, we assume that the long axis between the two cells is nearly parallel, and that their positions are sufficiently close at the initial time because we observe the dynamics two ECs after cell division. The initial position r_i^0 and orientation angle ψ_i^0 ($i = 1, 2$) are randomly selected in accordance with a uniform distribution $r_1^0 \in [-1.0, 1.0] \times [-7.5, 12.5]$, $r_2^0 \in [-1.0, 1.0] \times [7.5, 12.5]$, $\psi_i^0 \in [-0.05\pi, 0.05\pi]$, respectively. As the two cells migrate in opposite directions after cell division, we set opposite initial velocities $v_i^0 = v_{i,0}(\cos \psi_i^0, \sin \psi_i^0)$, where $v_{1,0}$ and $v_{2,0}$ follow the uniform distributions [0.3, 0.5] and [-0.5, -0.3], respectively.

In simulations of the dynamics of multiple ECs, 1000 ECs are distributed at random within a box region $[0, 2500] \times [0, 200]$ at $t = 0$ and one EC is supplied every ten steps within this region. The number of ECs at time t is $N_t = 1000 + \lfloor t/10 \rfloor$, where $\lfloor x \rfloor$ is the largest integer which does not exceeds x. As for the boundary condition, we assume that ECs cannot pass through the box region's lower edge, and its right and left ends are connected (a periodic boundary condition). The initial velocity and orientation angle of each EC

are randomly selected according to uniform distribution $[-0.01, 0.01] \times [-0.01, 0.01]$ and $[-\pi/2, \pi/2)$, respectively. In the simulation of mixing wild-type and KO cells, the initial 1000 cells are separated into Wild-type and KO cells according to the mixing ratio. Then, Wild-type or KO cells were supplied every ten steps with a probability dependent on the mixing ratio. For example, when the mixing ratio is Wild-type:KO = 4:1, wild-type cells appear with a probability of 0.8 and KO cells with a probability of 0.2. Numerical simulation and data analysis were executed in Fortran 90 and Mathematica 13.1 (Wolfram Research, Inc., Champaign, US).